Nonlinear mechanics of beams with partial piezoelectric layers

Hamed Farokhi [a], Mergen H. Ghayesh [b,*]

[a] *Department of Mechanical and Construction Engineering, Northumbria University, Newcastle upon Tyne NE1 8ST, UK*
[b] *School of Mechanical Engineering, University of Adelaide, South Australia 5005, Australia*
**Corresponding author: mergen.ghayesh@adelaide.edu.au*
Email: (H Farokhi): hamed.farokhi@northumbria.ac.uk

Abstract

This paper investigates the nonlinear static response as well as nonlinear forced dynamics of a clamped-clamped beam actuated by piezoelectric patches partially covering the beam from both sides. This study is the first to develop a high-dimensional nonlinear model for such piezoelectric-beam configuration. The nonlinear dynamical resonance characteristics of the electromechanical system is examined under simultaneous DC and AC piezoelectric actuations, while highlighting the effects of modal energy transfer and internal resonances. A multi-physics coupled model of the beam-piezoelectric system is proposed based on the nonlinear beam theory of Bernoulli-Euler and the piezoelectric constitutive equations. The discretised model of the system is obtained with the help of the Galerkin weighted residual technique while retaining 32 degrees of freedom. Three-dimensional finite element analysis is conducted as well in the static regime to validate the developed model and numerical simulation. It is shown that the response of the system in the nonlinear resonant region is strongly affected by a three-to-one internal resonance.

Keywords: Nonlinear mechanics; Piezoelectric layer; Coupled; Bending

1. Introduction

Actuated plate and beam structures are present in many mechanical systems [1-8]. Among them, piezoelectric materials [9-12] are in many engineering systems and are used for different applications involving sensing and actuation ranging from macro systems to microsystems. For instance, they are utilized for active vibration control, precise position adjustment and control, different types of energy harvesting, and static and dynamic actuations. The presence of geometric nonlinearities as well as the coupled electromechanical nature of piezoelectric materials makes the analysis and modelling of these systems more challenging.

There are many studies in the literature on the utilisation of piezoelectrics in actuation, control, sensing, and energy harvesting [13-21]. For instance, Lee et al. [22] designed an RF (radio-frequency) microelectromechanical system (MEMS) operating based on piezoelectric actuation. Narita et al. [23] examined the nonlinear static bending response of composite actuators of piezoelectric type both analytically and experimentally. The linear flexural response of a piezoelectrically actuated Bernoulli-Euler beam was investigated by Want and Quek [24]. Further investigations were conducted by Kumar and Narayanan [14], who employed a finite element technique to study the vibration control of a beam by optimising the position of the actuator and sensor of piezoelectric type. Bowen et al. [25] conducted finite element analysis to study the jump phenomenon in asymmetric laminates under piezoelectric actuation and compared it to experimental results. Ghazavi et al. [26] continued the investigations by analysing the stability of the transverse motion of a microcantilever under piezoelectric actuation. Mahmoodi et al. [27] investigated the subharmonic resonance vibrations of a piezoelectrically actuated microcantilever employing

an analytical perturbation technique along with a one-mode Galerkin discretisation. Further analysis was performed by Xiao et al. [28], who studied the pull-in instability of a MEMS device with piezoelectric layers under electrostatic actuation. All of the mentioned valuable investigations examined the response of the system using single-mode/low-dimensional models or using experimental techniques.

This study develops a nonlinear high-dimensional electromechanical model for a bimorph configuration of a piezoelectrically actuated clamped-clamped beam for the first time and investigates the nonlinear static and dynamic responses of the system. The proposed nonlinear model is verified through comparison to three-dimensional nonlinear finite element analysis. The verified model is used to examine the nonlinear resonance characteristics and the nonlinear dynamical behaviour of the piezoelectrically actuated system while highlighting the effect of modal coupling and internal resonances. The numerical results are presented through constructing frequency- and force-amplitude plots, time histories, phase-plane diagrams, and Poincaré sections.

2. Coupled electromechanical model development

In this section, the geometrically nonlinear model of the piezoelectrically actuated beam is derived using the Bernoulli-Euler beam and the piezoelectric constitutive equations. The schematic of the system is shown in Fig. 1, with beam dimensions shown as L, b, and t_b, for length, width, and thickness respectively. The thicknesses of the top and bottom piezoelectric patches are shown by $t_p^{(1)}$ and $t_p^{(2)}$, respectively. Throughout this section, the superscript (1) denotes dimensions or properties of the top piezoelectric patch while the

superscript (2) denotes those of the bottom piezoelectric patch. It is assumed that the width of the piezoelectric patches are the same as that of the beam and that both patches cover the same portion of the beam, i.e. are of same length l_2-l_1. A rectangular coordinate system is utilised to describe the motion of the system, with z and $w(x,t)$ denoting the transverse direction and transverse displacement, and x and $u(x,t)$ representing the axial direction and axial displacement.

The nonzero displacement vector components for the employed beam model can be written as

$$U_x(t,x,z)=u(t,x)-\begin{cases} z\dfrac{\partial}{\partial x}\left[w(t,x)\right], & x<l_1 \text{ or } x>l_2, \\ (z-z_n)\dfrac{\partial}{\partial x}\left[w(t,x)\right], & l_1\le x\le l_2, \end{cases}$$
$$U_z(t,x,z)=w(t,x) \tag{1}$$

in which z_n denotes the distance between the centreline and the neutral axis for the portion of the beam covered by piezoelectric layers.

The nonlinear axial strain for the beam and the piezoelectric patches can be expressed as

$$\begin{cases} x<l_1 \text{ or } x>l_2 & \Rightarrow \quad \varepsilon_{xx}=\varepsilon_1=\varepsilon_0-z\kappa, \\ l_1\le x\le l_2 & \Rightarrow \quad \varepsilon_{xx}=\varepsilon_1=\varepsilon_0-(z-z_n)\kappa, \end{cases} \tag{2}$$

where

$$\varepsilon_0=\frac{\left[\dfrac{\partial w(t,x)}{\partial x}\right]^2}{2}+\frac{\partial u(t,x)}{\partial x}, \quad \kappa=\frac{\partial^2 w(t,x)}{\partial x^2}, \tag{3}$$

in which the nonlinear term is due to the stretching of the centreline.

Having obtained the expression for the axial strain, the beam axial stress can be obtained as $\sigma_b = E_b \varepsilon_{xx}$, where E_b is the beam's Young's modulus.

For the piezoelectric layers, the one-dimensional form of the constitutive equations can be written as

$$\begin{cases} \sigma_p^{(k)} = c_{11}^{(k)} \varepsilon_1^{(k)} - h_{31}^{(k)} D_3^{(k)}, \\ \\ E_3^{(k)} = -h_{31}^{(k)} \varepsilon_1^{(k)} + \beta_{33}^{(k)} D_3^{(k)}, \end{cases} \qquad k = 1,2, \tag{4}$$

in which the subscripts 1 and 3 represent the *x* and *z* directions, respectively, and the superscript denote the top piezoelectric patch when *k*=1 and the bottom one when *k*=2. $c_{11}^{(k)}$ stands for the piezoelectric elastic stiffness while $D_3^{(k)}$ and $E_3^{(k)}$ denote the electric displacement and the electric field in the *z* direction, respectively. Additionally, $\beta_{33}^{(k)}$ is the impermittivity constant. $h_{31}^{(k)}$ is another piezoelectric constant. It should be noted that the poling direction for both piezoelectric patches is considered to be in the positive *z* direction.

The variation of the strain energy can be written for the beam layer as

$$\begin{aligned} \delta \Pi_{\text{beam}} = & \int_0^{l_1} \int_{A_b} E_b \left(\varepsilon_0 - z\kappa\right)\left(\delta\varepsilon_0 - z\delta\kappa\right) \mathrm{d}A\mathrm{d}x + \int_{l_1}^{l_2} \int_{A_b} E_b \left[\varepsilon_0 - \left(z - z_n\right)\kappa\right]\left[\delta\varepsilon_0 - \left(z - z_n\right)\delta\kappa\right] \mathrm{d}A\mathrm{d}x \\ & + \int_{l_2}^{L} \int_{A_b} E_b \left(\varepsilon_0 - z\kappa\right)\left(\delta\varepsilon_0 - z\delta\kappa\right) \mathrm{d}A\mathrm{d}x, \end{aligned} \tag{5}$$

in which A_b denotes the beam cross-sectional area and δ denotes the variational operator. After some mathematical manipulations, the variation of the beam potential energy can be written in the following form:

$$\delta\Pi_{\text{beam}} = \int_0^L \Bigg\{ E_b A_b \left(\frac{1}{2}\left(\frac{\partial w}{\partial x}\right)^2 + \frac{\partial u}{\partial x} \right)\left(\frac{\partial w}{\partial x}\delta\left(\frac{\partial w}{\partial x}\right) + \delta\left(\frac{\partial u}{\partial x}\right)\right) + E_b I_b \frac{\partial^2 w}{\partial x^2}\delta\left(\frac{\partial^2 w}{\partial x^2}\right)$$
$$+ G(x)\Bigg[E_b A_b z_n \left(\frac{1}{2}\left(\frac{\partial w}{\partial x}\right)^2 + \frac{\partial u}{\partial x} \right)\delta\left(\frac{\partial^2 w}{\partial x^2}\right) + E_b A_b z_n^2 \frac{\partial^2 w}{\partial x^2}\delta\left(\frac{\partial^2 w}{\partial x^2}\right)$$
$$+ E_b A_b z_n \frac{\partial^2 w}{\partial x^2}\left(\delta\left(\frac{\partial u}{\partial x}\right) + \frac{\partial w}{\partial x}\delta\left(\frac{\partial w}{\partial x}\right)\right)\Bigg]\Bigg\} \mathrm{d}x, \tag{6}$$

in which I_b denotes the beam second moment of area with respect the centreline. Additionally, $G(x) = Hv(x - l_1) - Hv(x - l_2)$, in which Hv represents the Heaviside function.

The strain energy of the piezoelectric patches, in variational form, can be written as

$$\delta\Pi_{\text{piezo}}^{(k)} = \int_{l_1}^{l_2} \int_{A_p^{(k)}} \left[\left(c_{11}^{(k)} \varepsilon_1^{(k)} - h_{31}^{(k)} D_3^{(k)} \right)\left[\delta\varepsilon_0 - (z - z_n)\delta\kappa \right] + \left(-h_{31}^{(k)} \varepsilon_1^{(k)} + \beta_{33}^{(k)} D_3^{(k)} \right)\delta D_3^{(k)} \right] \mathrm{d}A\,\mathrm{d}x, \tag{7}$$

which can be expanded for each piezoelectric layer as

$$\begin{aligned}
\delta\Pi_{\text{piezo}}^{(1)} &= c_{11}^{(1)} A_p^{(1)} \int_{l_1}^{l_2} \left(\frac{1}{2}\left(\frac{\partial w}{\partial x}\right)^2 + \frac{\partial u}{\partial x} \right)\left(\frac{\partial w}{\partial x}\delta\left(\frac{\partial w}{\partial x}\right) + \delta\left(\frac{\partial u}{\partial x}\right)\right)\mathrm{d}x \\
&+ c_{11}^{(1)} A_p^{(1)} \left[z_n - \frac{1}{2}\left(t_b + t_p^{(1)} \right) \right] \int_{l_1}^{l_2} \left[\left(\frac{1}{2}\left(\frac{\partial w}{\partial x}\right)^2 + \frac{\partial u}{\partial x} \right)\delta\left(\frac{\partial^2 w}{\partial x^2}\right) + \frac{\partial^2 w}{\partial x^2}\left(\frac{\partial w}{\partial x}\delta\left(\frac{\partial w}{\partial x}\right) + \delta\left(\frac{\partial u}{\partial x}\right)\right)\right]\mathrm{d}x \\
&+ \frac{1}{3} c_{11}^{(1)} b \left[\left(t_p^{(1)} \right)^3 + 3 t_p^{(1)} \left(\frac{t_b}{2} - z_n \right)^2 + 3\left(t_p^{(1)} \right)^2 \left(\frac{t_b}{2} - z_n \right) \right] \int_{l_1}^{l_2} \frac{\partial^2 w}{\partial x^2}\delta\left(\frac{\partial^2 w}{\partial x^2}\right)\mathrm{d}x \\
&- h_{31}^{(1)} A_p^{(1)} \int_{l_1}^{l_2} D_3^{(1)} \left(\frac{\partial w}{\partial x}\delta\left(\frac{\partial w}{\partial x}\right) + \delta\left(\frac{\partial u}{\partial x}\right)\right)\mathrm{d}x + h_{31}^{(1)} A_p^{(1)} \left[\frac{1}{2}\left(t_b + t_p^{(1)} \right) - z_n \right] \int_{l_1}^{l_2} D_3^{(1)} \delta\left(\frac{\partial^2 w}{\partial x^2}\right)\mathrm{d}x \\
&- h_{31}^{(1)} A_p^{(1)} \int_{l_1}^{l_2} \left(\frac{1}{2}\left(\frac{\partial w}{\partial x}\right)^2 + \frac{\partial u}{\partial x} \right)\delta D_3^{(1)}\,\mathrm{d}x + \beta_{33}^{(1)} A_p^{(1)} \int_{l_1}^{l_2} D_3^{(1)} \delta D_3^{(1)}\,\mathrm{d}x \\
&+ h_{31}^{(1)} A_p^{(1)} \left[\frac{1}{2}\left(t_b + t_p^{(1)} \right) - z_n \right] \int_{l_1}^{l_2} \frac{\partial^2 w}{\partial x^2}\delta D_3^{(1)}\,\mathrm{d}x,
\end{aligned} \tag{8}$$

$$
\begin{aligned}
\delta \Pi_{\text{piezo}}^{(2)} &= c_{11}^{(2)} A_p^{(2)} \int_{l_1}^{l_2} \left(\frac{1}{2}\left(\frac{\partial w}{\partial x} \right)^2 + \frac{\partial u}{\partial x} \right) \left(\frac{\partial w}{\partial x} \delta\left(\frac{\partial w}{\partial x} \right) + \delta\left(\frac{\partial u}{\partial x} \right) \right) \mathrm{d}x \\
&+ c_{11}^{(2)} A_p^{(2)} \left[z_n + \frac{1}{2}\left(t_b + t_p^{(2)} \right) \right] \int_{l_1}^{l_2} \left[\left(\frac{1}{2}\left(\frac{\partial w}{\partial x} \right)^2 + \frac{\partial u}{\partial x} \right) \delta\left(\frac{\partial^2 w}{\partial x^2} \right) + \frac{\partial^2 w}{\partial x^2} \left(\frac{\partial w}{\partial x} \delta\left(\frac{\partial w}{\partial x} \right) + \delta\left(\frac{\partial u}{\partial x} \right) \right) \right] \mathrm{d}x \\
&+ \frac{1}{3} c_{11}^{(2)} b \left[\left(t_p^{(2)} \right)^3 + 3 t_p^{(2)} \left(\frac{t_b}{2} + z_n \right)^2 + 3\left(t_p^{(2)} \right)^2 \left(\frac{t_b}{2} + z_n \right) \right] \int_{l_1}^{l_2} \frac{\partial^2 w}{\partial x^2} \delta\left(\frac{\partial^2 w}{\partial x^2} \right) \mathrm{d}x \\
&- h_{31}^{(2)} A_p^{(2)} \int_{l_1}^{l_2} D_3^{(2)} \left(\frac{\partial w}{\partial x} \delta\left(\frac{\partial w}{\partial x} \right) + \delta\left(\frac{\partial u}{\partial x} \right) \right) \mathrm{d}x + h_{31}^{(2)} A_p^{(2)} \left[-\frac{1}{2}\left(t_b + t_p^{(2)} \right) - z_n \right] \int_{l_1}^{l_2} D_3^{(2)} \delta\left(\frac{\partial^2 w}{\partial x^2} \right) \mathrm{d}x \\
&- h_{31}^{(2)} A_p^{(2)} \int_{l_1}^{l_2} \left(\frac{1}{2}\left(\frac{\partial w}{\partial x} \right)^2 + \frac{\partial u}{\partial x} \right) \delta D_3^{(2)} \, \mathrm{d}x + \beta_{33}^{(2)} A_p^{(2)} \int_{l_1}^{l_2} D_3^{(2)} \delta D_3^{(2)} \, \mathrm{d}x \\
&+ h_{31}^{(2)} A_p^{(2)} \left[-\frac{1}{2}\left(t_b + t_p^{(2)} \right) - z_n \right] \int_{l_1}^{l_2} \frac{\partial^2 w}{\partial x^2} \delta D_3^{(2)} \, \mathrm{d}x,
\end{aligned}
\tag{9}
$$

in which $A_p^{(1)}$ and $A_p^{(2)}$ denote the area of the cross section of the top and bottom piezoelectric layers, respectively.

The layered system kinetic energy variation be written as

$$
\begin{aligned}
\delta KE &= \int_0^L M(x) \left[\frac{\partial}{\partial t}(\delta w) \frac{\partial w}{\partial t} + \frac{\partial}{\partial t}(\delta u) \frac{\partial u}{\partial t} \right] \mathrm{d}x, \\
M(x) &= \rho_b A_b + G(x)\left(\rho_p^{(1)} A_p^{(1)} + \rho_p^{(2)} A_p^{(2)} \right),
\end{aligned}
\tag{10}
$$

where ρ_b is the beam mass density, while $\rho_p^{(1)}$ and $\rho_p^{(2)}$ denote the mass density of the top and bottom piezoelectric layers, respectively.

In the present study, an input voltage of $V^{(1)}(x,t)$ is applied to the top surface of the top layer of piezoelectric and an input voltage of $V^{(2)}(x,t)$ is applied to the bottom surface of the bottom layer. The resultant electrical virtual work can be formulated as

$$
\delta W_{ext} = b \int_0^L \left[V^{(2)}(t,x) \delta D_3^{(2)}(t,x) \right] \mathrm{d}x - b \int_0^L \left[V^{(1)}(t,x) \delta D_3^{(1)}(t,x) \right] \mathrm{d}x. \tag{11}
$$

The virtual work of the damping can be written as

$$\begin{aligned}\delta W_v &= -\frac{1}{A_b}\int_V c_d(x)\left[\delta w\frac{\partial w}{\partial t}+\delta u\frac{\partial u}{\partial t}\right]\mathrm{d}V \\ &= \int_0^L\left[c_d^b+\left(c_d^{p_1}\frac{A_p^{(1)}}{A_b}+c_d^{p_2}\frac{A_p^{(2)}}{A_b}\right)G(x)\right]\left[\delta w\frac{\partial w}{\partial t}+\delta u\frac{\partial u}{\partial t}\right]\mathrm{d}x,\end{aligned} \tag{12}$$

where c_d^b, $c_d^{p_1}$, and $c_d^{p_2}$ are respectively the beam, top piezoelectric, and bottom piezoelectric layers damping coefficients.

The equations of motion of the electromechanical system can be derived as

$$\begin{aligned}&M(x)\frac{\partial^2 u}{\partial t^2}+c_d(x)\frac{\partial u}{\partial t}-\frac{\partial}{\partial x}\left[e(x)\left(\frac{1}{2}\left(\frac{\partial w}{\partial x}\right)^2+\frac{\partial u}{\partial x}\right)\right]-\frac{\partial}{\partial x}\left[f(x)\frac{\partial^2 w}{\partial x^2}\right] \\ &+\frac{\partial}{\partial x}\left[D_3^{(1)}h_2^{(1)}(x)+D_3^{(2)}h_2^{(2)}(x)\right]=0,\end{aligned} \tag{13}$$

$$\begin{aligned}&M(x)\frac{\partial^2 w}{\partial t^2}+\frac{\partial^2}{\partial x^2}\left[C(x)\frac{\partial^2 w}{\partial x^2}\right]+c_d(x)\frac{\partial w}{\partial t}-\frac{\partial}{\partial x}\left[e(x)\left(\frac{\partial w}{\partial x}\right)\left(\frac{1}{2}\left(\frac{\partial w}{\partial x}\right)^2+\frac{\partial u}{\partial x}\right)\right] \\ &-\frac{\partial}{\partial x}\left[f(x)\left(\frac{\partial w}{\partial x}\frac{\partial^2 w}{\partial x^2}\right)\right]+\frac{\partial^2}{\partial x^2}\left[f(x)\left(\frac{1}{2}\left(\frac{\partial w}{\partial x}\right)^2+\frac{\partial u}{\partial x}\right)\right] \\ &+\frac{\partial^2}{\partial x^2}\left[D_3^{(1)}h_1^{(1)}(x)+D_3^{(2)}h_1^{(2)}(x)\right]+\frac{\partial}{\partial x}\left[\left(\frac{\partial w}{\partial x}\right)\left(D_3^{(1)}h_2^{(1)}(x)+D_3^{(2)}h_2^{(2)}(x)\right)\right]=0,\end{aligned} \tag{14}$$

$$h_1^{(1)}(x)\frac{\partial^2 w}{\partial x^2}-h_2^{(1)}(x)\left(\frac{\partial u}{\partial x}+\frac{1}{2}\left(\frac{\partial w}{\partial x}\right)^2\right)+\beta^{(1)}(x)D_3^{(1)}+bV^{(1)}(t,x)=0, \tag{15}$$

$$h_1^{(2)}(x)\frac{\partial^2 w}{\partial x^2}-h_2^{(2)}(x)\left(\frac{\partial u}{\partial x}+\frac{1}{2}\left(\frac{\partial w}{\partial x}\right)^2\right)+\beta^{(2)}(x)D_3^{(2)}-bV^{(2)}(t,x)=0. \tag{16}$$

in which

$$C(x)=E_bI_b+G(x)\left\{E_bA_bz_n^2+\frac{1}{3}c_{11}^{(1)}b\left[\left(t_p^{(1)}\right)^3+3t_p^{(1)}\left(\frac{t_b}{2}-z_n\right)^2+3\left(t_p^{(1)}\right)^2\left(\frac{t_b}{2}-z_n\right)\right]\right.$$
$$\left.+\frac{1}{3}c_{11}^{(2)}b\left[\left(t_p^{(2)}\right)^3+3t_p^{(2)}\left(\frac{t_b}{2}+z_n\right)^2+3\left(t_p^{(2)}\right)^2\left(\frac{t_b}{2}+z_n\right)\right]\right\}$$

$$e(x)=E_bA_b+G(x)\left(c_{11}^{(1)}A_p^{(1)}+c_{11}^{(2)}A_p^{(2)}\right),$$

$$f(x)=E_bA_bz_n+G(x)\left\{c_{11}^{(1)}A_p^{(1)}\left[z_n-\frac{1}{2}\left(t_b+t_p^{(1)}\right)\right]+c_{11}^{(2)}A_p^{(2)}\left[z_n+\frac{1}{2}\left(t_b+t_p^{(2)}\right)\right]\right\},$$

$$h_1^{(1)}(x)=G(x)h_{31}^{(1)}A_p^{(1)}\left[\frac{1}{2}\left(t_b+t_p^{(1)}\right)-z_n\right],\qquad h_1^{(2)}(x)=G(x)h_{31}^{(2)}A_p^{(2)}\left[-\frac{1}{2}\left(t_b+t_p^{(2)}\right)-z_n\right],$$

$$h_2^{(1)}(x)=G(x)h_{31}^{(1)}A_p^{(1)},\qquad h_2^{(2)}(x)=G(x)h_{31}^{(2)}A_p^{(2)},$$

$$\beta^{(1)}(x)=G(x)A_p^{(1)}\beta_{33}^{(1)},\qquad \beta^{(2)}(x)=G(x)A_p^{(2)}\beta_{33}^{(2)},$$

$$V^{(1)}(t,x)=G(x)V^{(1)}(t),\qquad V^{(2)}(t,x)=G(x)V^{(2)}(t). \tag{17}$$

Calculating $D_3^{(1)}$ and $D_3^{(2)}$ in terms of input voltage and displacements using Eqs. (15) and (16) and substituting into Eqs. (13) and (14) yields

$$M(x)\frac{\partial^2u}{\partial t^2}+c_d(x)\frac{\partial u}{\partial t}-\frac{\partial}{\partial x}\left[\left(e(x)-\frac{\left(h_2^{(1)}(x)\right)^2}{\beta^{(1)}(x)}-\frac{\left(h_2^{(2)}(x)\right)^2}{\beta^{(2)}(x)}\right)\left(\frac{\partial u}{\partial x}+\frac{1}{2}\left(\frac{\partial w}{\partial x}\right)^2\right)\right]$$
$$-\frac{\partial}{\partial x}\left[\left(\frac{h_1^{(1)}(x)h_2^{(1)}(x)}{\beta^{(1)}(x)}+\frac{h_1^{(2)}(x)h_2^{(2)}(x)}{\beta^{(2)}(x)}+f(x)\right)\frac{\partial^2w}{\partial x^2}\right] \tag{18}$$
$$+\frac{\partial}{\partial x}\left[V^{(2)}(x,t)\frac{bh_2^{(2)}(x)}{\beta^{(2)}(x)}-V^{(1)}(x,t)\frac{bh_2^{(1)}(x)}{\beta^{(1)}(x)}\right]=0,$$

$$
\begin{aligned}
&M(x)\frac{\partial^2 w}{\partial t^2}+c_d(x)\frac{\partial w}{\partial t}+\frac{\partial^2}{\partial x^2}\left[\frac{\partial^2 w}{\partial x^2}\left(C(x)-\frac{\left(h_1^{(1)}(x)\right)^2}{\beta^{(1)}(x)}-\frac{\left(h_1^{(2)}(x)\right)^2}{\beta^{(2)}(x)}\right)\right]\\
&\quad-\frac{\partial}{\partial x}\left[\left(e(x)-\frac{\left(h_2^{(1)}(x)\right)^2}{\beta^{(1)}(x)}-\frac{\left(h_2^{(2)}(x)\right)^2}{\beta^{(2)}(x)}\right)\left(\frac{\partial w}{\partial x}\right)\left(\frac{\partial u}{\partial x}+\frac{1}{2}\left(\frac{\partial w}{\partial x}\right)^2\right)\right]\\
&\quad+\frac{\partial^2}{\partial x^2}\left[\left(\frac{1}{2}\left(\frac{\partial w}{\partial x}\right)^2+\frac{\partial u}{\partial x}\right)\left(f(x)+\frac{h_2^{(1)}(x)}{\beta^{(1)}(x)}h_1^{(1)}(x)+\frac{h_2^{(2)}(x)}{\beta^{(2)}(x)}h_1^{(2)}(x)\right)\right]\\
&\quad-\frac{\partial}{\partial x}\left[\left(\frac{\partial^2 w}{\partial x^2}\frac{\partial w}{\partial x}\right)\left(\frac{h_2^{(1)}(x)}{\beta^{(1)}(x)}h_1^{(1)}(x)+\frac{h_2^{(2)}(x)}{\beta^{(2)}(x)}h_1^{(2)}(x)+f(x)\right)\right]\\
&\quad+\frac{\partial^2}{\partial x^2}\left[\frac{b}{\beta^{(2)}(x)}h_1^{(2)}(x)V^{(2)}(x,t)-\frac{b}{\beta^{(1)}(x)}h_1^{(1)}(x)V^{(1)}(x,t)\right]\\
&\quad+\frac{\partial}{\partial x}\left[\left(V^{(2)}(t,x)\frac{bh_2^{(2)}(x)}{\beta^{(2)}(x)}-V^{(1)}(t,x)\frac{bh_2^{(1)}(x)}{\beta^{(1)}(x)}\right)\left(\frac{\partial w}{\partial x}\right)\right]=0.
\end{aligned}
\tag{19}
$$

The developed model of the doubly clamped beam under piezoelectric actuation takes into account the geometric nonlinearities due to centreline stretching; furthermore, both axial and transverse motions are modelled and accounted for. In what follows, the Galerkin decomposition method is used to discretise equations of motion and recast them into a system of ordinary differential equations (ODEs). First, the axial and transverse motions are approximated as a series of time-dependent generalised coordinates multiplied by assumed spatial shape functions. Denoting the transverse and axial generalised coordinates by *q* and *r*, respectively, the axial and transverse displacements are defined as

$$
\begin{aligned}
u(t,x)&=\sum_{k=1}^{M} r_k(t)\Phi_k(x),\\
w(t,x)&=\sum_{k=1}^{N} q_k(t)\Psi_k(x),
\end{aligned}
\tag{20}
$$

where

$$\Phi_k(x)=\sin\left(\frac{k\pi x}{L}\right), \tag{21}$$

$$\begin{aligned}\Psi_k(x)&=-\left[\cos\left(\frac{\theta_k x}{L}\right)-\lambda_k\sin\left(\frac{\theta_k x}{L}\right)\right]+\left[\cosh\left(\frac{\theta_k x}{L}\right)-\lambda_k\sinh\left(\frac{\theta_k x}{L}\right)\right],\\ \lambda_k&=\left[\sinh(\theta_k)-\sin(\theta_k)\right]^{-1}\left[\cosh(\theta_k)-\cos(\theta_k)\right],\end{aligned} \tag{22}$$

in which θ_k denotes the *k*th root of $1-\cos(\theta)\cosh(\theta)=0$. Application of the Galerkin method gives a set of ODEs of dimension *M*+*N*. In the present study, 16 degrees of freedom are considered for each longitudinal and transverse displacements, i.e. *M*=*N*= 16, yielding a 32-DOF (degree-of-freedom) model. This high-dimensional discretised model is solved numerically through use of a continuation method and a time-integration technique.

3. Nonlinear static and dynamic responses

This section analyses the geometrically nonlinear electromechanical response of the system for two cases: (i) static piezoelectric actuations and (ii) simultaneous static and dynamic piezoelectric actuations. $V^{(1)}(t)$ and $V^{(2)}(t)$ are substituted by $V_s^{(1)}+V_d^{(1)}\cos\left(\omega_p^{(1)}t\right)$ and $V_s^{(2)}+V_d^{(2)}\cos\left(\omega_p^{(2)}t\right)$, respectively. To validate the developed theoretical model and the numerical simulations, a nonlinear static three-dimensional (3D) finite element analysis (FEA) is conducted using Abaqus. The numerical simulations are conducted for a piezoelectrically actuated system of dimensions t_b=0.6 mm, b=5.0 mm, L=120 mm, $t_p^{(1)}=t_p^{(2)}$ =0.3 mm , l_1=0.2L, and l_2=0.6L. The material properties of the beam layer are: E_b=70 GPa, Poisson's ratio ν_b=0.33, and ρ_b=2300 kg/m^3.

Both piezoelectric layers are assumed to be of type PZT-5H with a mass density of 7500 kg/m^3. The piezoelectric properties are listed in Table 1. The piezoelectric constants in Eq. (4) are formulated as functions of the constants reported in Table 1. For the present study, given that both layers are of the same material, the constants in Eq. (4) can be calculated as

$$\begin{aligned} c_{11}^{(1)} &= c_{11}^{(2)} = \left(s_{11} - d_{31}^2/\xi_{33}\right)^{-1} = 71.3973 \text{ GPa}, \\ h_{31}^{(1)} &= h_{31}^{(2)} = -\left(d_{31} - s_{11}\xi_{33}/d_{31}\right)^{-1} = -649.8374 \text{ MV/m}, \\ \beta_{33}^{(1)} &= \beta_{33}^{(2)} = \left(\xi_{33} - d_{31}^2/s_{11}\right)^{-1} = 39.1325 \text{ Mm/F}. \end{aligned} \tag{23}$$

It is important to note that since the thicknesses and material properties of both piezoelectric layers are the same, z_n=0.

3.1 Static piezoelectric actuation

The nonlinear response of the system under static piezoelectric actuation is examined in this section. To this end, the dynamic AC voltage amplitudes, i.e. $V_d^{(1)}$ and $V_d^{(2)}$, are set to zero and the DC voltage amplitudes, i.e. $V_s^{(1)}$ and $V_s^{(1)}$, are varied as the control parameter. In this study it is assumed that $V_s^{(1)} = V_s^{(2)} = V_s$. Additionally, a 3D finite element analysis is conducted using Abaqus/CAE for comparison and benchmark purposes. In order to ensure accurate 3D finite element analysis, a 20-node 3D element is used for beam layer (i.e. the C3D20R element) as well as the piezoelectric layers (i.e. the C3D20RE element), while accounting for geometric nonlinearities. A fine mesh of 0.3 mm, as shown in Fig. 2, is used for beam and piezoelectric layers to ensure converged results.

Figure 3(a) shows the displacement in the transverse direction at x/L=0.4 as a function of the DC input voltage obtained via the proposed model and that obtained using the 3D FEA. The figure shows that the proposed beam model predictions are in excellent agreement with those obtained via the 3D FEA. Figure 3(b) shows the deformed state of the system predicted by the two models. It is seen that, the present model gives very close predictions to those of the 3D FEA, verifying the reliability and accuracy of the proposed model and the employed numerical techniques. The detailed FEA results for transverse displacement and electric potential variation are illustrated in Fig. 4.

3.2 Simultaneous static and dynamic piezoelectric actuations

A nonlinear resonance dynamic analysis is performed in this section for a system under simultaneous static and dynamic piezoelectric actuations. More specifically, it is assumed that $V_s^{(1)} = V_s^{(2)} = V_s$ and $V_d^{(1)} = V_d^{(2)} = V_d$ and the system is under combined DC and AC actuation of $V_s + V_d \cos\left(\omega_p t\right)$. In the numerical simulations, several parameters namely the time (t), excitation frequency (ω_p), transverse natural frequencies ($\hat{\omega}_i$), and damping coefficient ($c_d = c_d^b = c_d^{p_1} = c_d^{p_2}$) are made dimensionless as

$$\begin{aligned}
&\tau = t\sqrt{\frac{E_b I_b}{\rho_b A_b L^4}},\\
&\Omega_p = \omega_p \sqrt{\frac{\rho_b A_b L^4}{E_b I_b}},\\
&\omega_i = \hat{\omega}_i \sqrt{\frac{\rho_b A_b L^4}{E_b I_b}} \quad i = 1,2,\\
&c_d^* = \frac{c_d L^4}{E_b I_b}\sqrt{\frac{E_b I_b}{\rho_b A_b L^4}}.
\end{aligned} \tag{24}$$

In the numerical calculations, c_d^* is substituted by $2\zeta\omega_1$; ζ denotes the damping ratio which is set to 0.006 in this study.

The present study focuses on the nonlinear resonance response of the piezoelectrically actuated system in the proximity of a three-to-one internal resonance. To this end, first the variation of the system natural frequencies with the input DC voltage is examined and plotted in Fig. 5. It is seen in sub-figure (a) that, the first transverse natural frequency of the system increases with increasing V_s. This is due to the fact that as the DC voltage is increased, the beam deforms and the beam centreline is stretched, hence stiffening the beam and increasing the natural frequency. Sub-figure (b) shows the variation ω_2/ω_1 ratio as a function of V_s; it is interesting to note that $\omega_2/\omega_1 \approx 3$ for V_s in the range of 480-580 V, hinting the possibility of the existence of an internal resonance of three-to-one.

To examine the resonance response of the system near $\omega_2/\omega_1 \approx 3$, Fig. 6 is constructed. For this figure, V_s = 560 V resulting in ω_2/ω_1 = 2.98; additionally, V_d is set to 10 V. As seen, the system shows a complicated nonlinear hardening-type resonance response, strongly affected by modal coupling and internal resonances. The appearance of hardening-type nonlinearity is due to the centreline stretching in the piezoelectric-beam system. Due to internal modal energy transfer, four saddle-node (SD) bifurcations appear in the primary resonance region. Additionally, it is seen that the system displays three torus (TR) bifurcations with quasiperiodic motion between TR_1 and TR_2 as well as between TR_3 and SD_3. The details of the quasiperiodic motion at Ω_p/ω_1 =1.06 is shown in Fig. 9, through time history, phase-plane plot and Poincaré section of the transverse displacement. The system shows stable periodic response elsewhere. The thin dashed lines connecting SD_1 and SD_2, as well as SD_3 and SD_4, indicate unstable attractors.

The details of the periodic motion at Ω_p/ω_1 = 1.0172 and 1.0703 are shown in Figs. 8 and 9, respectively, through time histories and phase-plane portraits. The transverse oscillations of the piezoelectrically actuated system again at Ω_p/ω_1 = 1.0172 and 1.0703 are shown in Fig. 10 for one period of oscillation. As seen, at Ω_p/ω_1 = 1.0172, the maximum transverse displacement occurs in the vicinity of x/L=0.4 while at Ω_p/ω_1 = 1.0703 it takes place around x/L=0.5. To better show the strong modal coupling and modal energy transfer in primary resonance region, Fig. 11 is constructed showing the resonance response of the first four transverse generalised coordinates of the system of Fig. 6.

The effect of the input DC voltage V_s on the nonlinear frequency-amplitude diagrams of the system is shown in Fig. 12. As seen, the resonance region shifts to the right on the frequency axis as V_s is increased, which is in fact due to increased natural frequency. It is interesting to note that there are almost no signs of internal resonance when V_s =300 V and 400 V. However, strong modal interactions are present for the case V_s = 500 V, showing both periodic (solid line) and quasiperiodic (thick dashed line) motions. As V_s is further increased to 600 V, again the modal interactions almost disappear. This figure shows the sensitivity of the internal resonances to the value of the DC input voltage.

In order to examine the effect of modal coupling and internal resonances on the force-amplitude response of the system, V_s is set to 580 V and Ω_p/ω_1 is set to 1.03 and then V_d is varied as the control parameter; the results are plotted in Fig. 13. As seen, the effect of internal resonances is visible, resulting in a complex force-amplitude response with four saddle-node bifurcations and two torus bifurcations. Additionally, the system shows stable quasiperiodic motion in between the two torus bifurcations and stable periodic motion elsewhere (indicated by solid line); the thin dashed lines show unstable motion. The force-

amplitude plots for the first four transverse generalised coordinates are shown in Fig. 14 to highlight the effect of modal internal energy transfer and internal resonances.

Figure 15, shows the force-amplitude plots for at different excitation frequency ratios; V_s is set to 580 V for all cases. It is see that as Ω_p/ω_1 ratio is increased, the modal interactions become stronger. Furthermore, quasiperiodic motion (indicated by thick dashed line) does not appear for the system with Ω_p/ω_1 = 1.01; however, as seen, quasiperiodic motion are present for larger frequency ratios; in fact, the range of quasiperiodic motion increases with increasing Ω_p/ω_1.

4. Concluding remarks

The nonlinear static and dynamic responses of a piezoelectrically actuated beam have been investigated numerically. A nonlinear continuous electromechanical model is developed describing the motion of the system under an applied input voltage. A high-dimensional discretised model is constructed via the Galerkin method; this set is solved numerically employing different techniques.

Comparing the nonlinear static behaviour of the system obtained via the proposed model to that obtained via nonlinear 3D FEA showed that the developed model is very accurate and reliable. The numerical results for the nonlinear forced resonant response of the beam under simultaneous DC and AC piezoelectric actuations showed complex resonance responses with strong modal interactions. In fact, it was shown that for a specific range of DC voltages, a three-to-one internal resonance exists between the first two modes, which alters the resonance response characteristics significantly. More specifically, the presence of internal resonance causes additional solution branches and extra peaks in the resonance region. Furthermore, due to presence of strong internal resonances, torus bifurcations occur in the primary resonance region giving rise to quasiperiodic motion. Examining the effect of the DC input voltage showed that as a result of increased V_s, the resonance region shifts to the right on the frequency axis. It was shown that as a result of a 16% change in the V_s, the internal resonances almost disappear from the resonance region. The force-amplitude plots of the system also clearly showed the strong effect of internal resonances, causing extra bifurcation points and giving rise to quasiperiodic motion.

Appendix A. Significance of discretised model's dimension

This section analyses the effect of the discretised model's dimension on nonlinear transverse deformation of the piezoelectrically actuated beam system. To this end, Fig. 16 is constructed, which is a counterpart of Fig. 3(b), showing the nonlinear transverse deformation obtained using three discretised models of dimensions 4, 16, and 32. As seen, the model consisting of 4 modes gives very inaccurate predictions. The 16-mode model gives better prediction than the 4-mode but still does not give converged results. The 32-mode model used in the present study, on the other hand, gives converged results. Hence, Fig. 16 highlights the significance of the number of modes when examining the nonlinear behaviour of clamped-clamped piezoelectrically actuated beams.

References

[1] Bayat, A., and Gaitanaros, S., 2019, "Elastic wave propagation in open-cell foams," Journal of Applied Mechanics, Transactions ASME, 86(5).

[2] Fang, X., Chuang, K. C., Jin, X., and Huang, Z., 2018, "Band-gap properties of elastic metamaterials with inerter-based dynamic vibration absorbers," Journal of Applied Mechanics, Transactions ASME, 85(7).

[3] Goodpaster, B. A., and Harne, R. L., 2018, "Analytical modeling and impedance characterization of the nonlinear dynamics of thermomechanically coupled structures," Journal of Applied Mechanics, Transactions ASME, 85(8).

[4] Kozuch, C. D., and Jasiuk, I. M., 2018, "Optimization of structures made from composites with elliptical inclusions," Journal of Applied Mechanics, Transactions ASME, 85(12).

[5] Louhghalam, A., Pellenq, R. J. M., and Ulm, F. J., 2018, "Thermalizing and damping in structural dynamics," Journal of Applied Mechanics, Transactions ASME, 85(8).

[6] Prasad, R., and Sarkar, A., 2019, "Broadband vibration isolation for rods and beams using periodic structure theory," Journal of Applied Mechanics, Transactions ASME, 86(2).

[7] Vatankhahghadim, B., and Damaren, C. J., 2019, "Deployment of a membrane attached to two axially moving beams," Journal of Applied Mechanics, Transactions ASME, 86(3).

[8] Nakamura, T., 2019, "Local stress-field reconstruction around holes in a plate using strain monitoring data and stress function," Journal of Applied Mechanics, Transactions ASME, 86(3).

[9] Liu, S., Ha, T., and Lu, N., 2019, "Experimentally and numerically validated analytical solutions to nonbuckling piezoelectric serpentine ribbons," Journal of Applied Mechanics, Transactions ASME, 86(5).

[10] Luo, Y., Zhang, C., Chen, W., and Yang, J., 2019, "Piezotronic effect of a thin film with elastic and piezoelectric semiconductor layers under a static flexural loading," Journal of Applied Mechanics, Transactions ASME, 86(5).

[11] Yuan, T. C., Yang, J., and Chen, L. Q., 2018, "Nonparametric identification of nonlinear piezoelectric mechanical systems," Journal of Applied Mechanics, Transactions ASME, 85(11).

[12] Zhang, H., Shen, M., Zhang, Y., Chen, Y., and Lü, C., 2018, "Identification of Static Loading Conditions Using Piezoelectric Sensor Arrays," Journal of Applied Mechanics, Transactions ASME, 85(1).

[13] Irschik, H., 2002, "A review on static and dynamic shape control of structures by piezoelectric actuation," Engineering Structures, 24(1), pp. 5-11.

[14] Kumar, K. R., and Narayanan, S., 2008, "Active vibration control of beams with optimal placement of piezoelectric sensor/actuator pairs," Smart Materials and Structures, 17(5), p. 055008.

[15] Raja, S., Prathap, G., and Sinha, P., 2002, "Active vibration control of composite sandwich beams with piezoelectric extension-bending and shear actuators," Smart Materials and Structures, 11(1), p. 63.

[16] Vasques, C., and Rodrigues, J. D., 2006, "Active vibration control of smart piezoelectric beams: comparison of classical and optimal feedback control strategies," Computers & structures, 84(22-23), pp. 1402-1414.

[17] Halim, M. A., and Park, J. Y., 2014, "Theoretical modeling and analysis of mechanical impact driven and frequency up-converted piezoelectric energy harvester for low-frequency and wide-bandwidth operation," Sensors and Actuators A: Physical, 208, pp. 56-65.

[18] Hu, G., Tang, L., and Das, R., 2017, "An impact-engaged two-degrees-of-freedom Piezoelectric Energy Harvester for Wideband Operation," Procedia Engineering, 173, pp. 1463-1470.

[19] Huicong, L., Chengkuo, L., Takeshi, K., Cho Jui, T., and Chenggen, Q., 2012, "Investigation of a MEMS piezoelectric energy harvester system with a frequency-widened-bandwidth mechanism introduced by mechanical stoppers," Smart Materials and Structures, 21(3), p. 035005.

[20] Liu, H., Lee, C., Kobayashi, T., Tay, C. J., and Quan, C., 2012, "Piezoelectric MEMS-based wideband energy harvesting systems using a frequency-up-conversion cantilever stopper," Sensors and Actuators A: Physical, 186, pp. 242-248.

[21] Liu, S., Cheng, Q., Zhao, D., and Feng, L., 2016, "Theoretical modeling and analysis of two-degree-of-freedom piezoelectric energy harvester with stopper," Sensors and Actuators A: Physical, 245, pp. 97-105.

[22] Lee, H.-C., Park, J.-H., Park, J.-Y., Nam, H.-J., and Bu, J.-U., 2005, "Design, fabrication and RF performances of two different types of piezoelectrically actuated Ohmic MEMS switches," Journal of micromechanics and microengineering, 15(11), p. 2098.

[23] Narita, F., Shindo, Y., and Mikami, M., 2005, "Analytical and experimental study of nonlinear bending response and domain wall motion in piezoelectric laminated actuators under ac electric fields," Acta Materialia, 53(17), pp. 4523-4529.

[24] Wang, Q., and Quek, S. T., 2000, "Flexural vibration analysis of sandwich beam coupled with piezoelectric actuator," Smart Materials and Structures, 9(1), p. 103.

[25] Bowen, C. R., Giddings, P. F., Salo, A. I., and Kim, H. A., 2011, "Modeling and characterization of piezoelectrically actuated bistable composites," IEEE transactions on ultrasonics, ferroelectrics, and frequency control, 58(9), pp. 1737-1750.

[26] Ghazavi, M.-R., Rezazadeh, G., and Azizi, S., 2010, "Pure parametric excitation of a micro cantilever beam actuated by piezoelectric layers," Applied Mathematical Modelling, 34(12), pp. 4196-4207.

[27] Mahmoodi, S. N., Jalili, N., and Ahmadian, M., 2010, "Subharmonics analysis of nonlinear flexural vibrations of piezoelectrically actuated microcantilevers," Nonlinear Dynamics, 59(3), pp. 397-409.

[28] Xiao, Y., Wang, B., and Zhou, S., 2015, "Pull-in voltage analysis of electrostatically actuated MEMS with piezoelectric layers: a size-dependent model," Mechanics Research Communications, 66, pp. 7-14.

Table 1. Piezoelectric material properties (PZT-5H)

Compliance constants (pm^2/N):
s_{11}=16.5
s_{12}=-4.78
s_{13}=-8.45
s_{33}=20.7
s_{44}=43.5
Piezoelectric constans (pm/V):
d_{31}=-274
d_{33}=593
d_{15}=741
Relative permittivity constants (ξ_0 = 8.8542 pF/m):
ξ_{11}/ξ_0 = 3130
ξ_{33}/ξ_0 = 3400

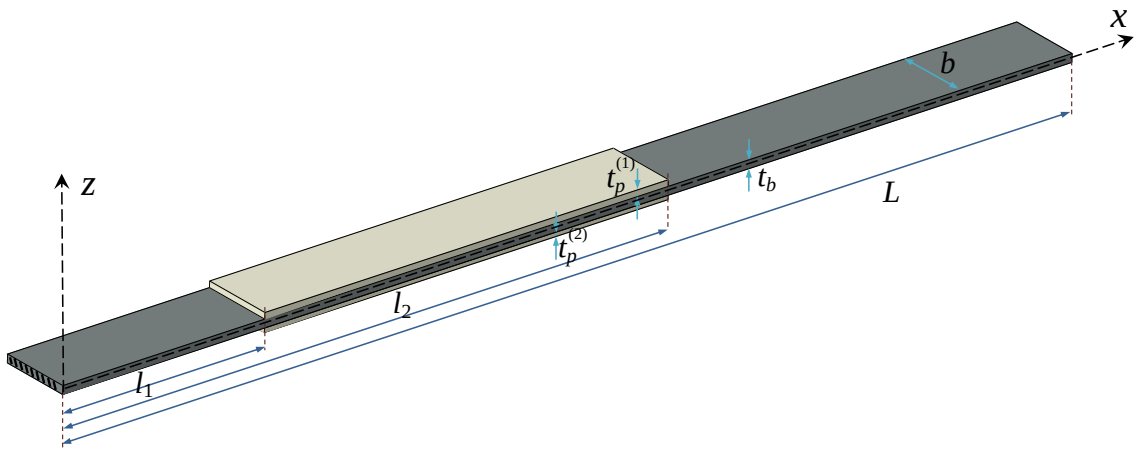

Fig.1. Schematic of a clamped-clamped beam partially covered by piezoelectric layers from both sides.

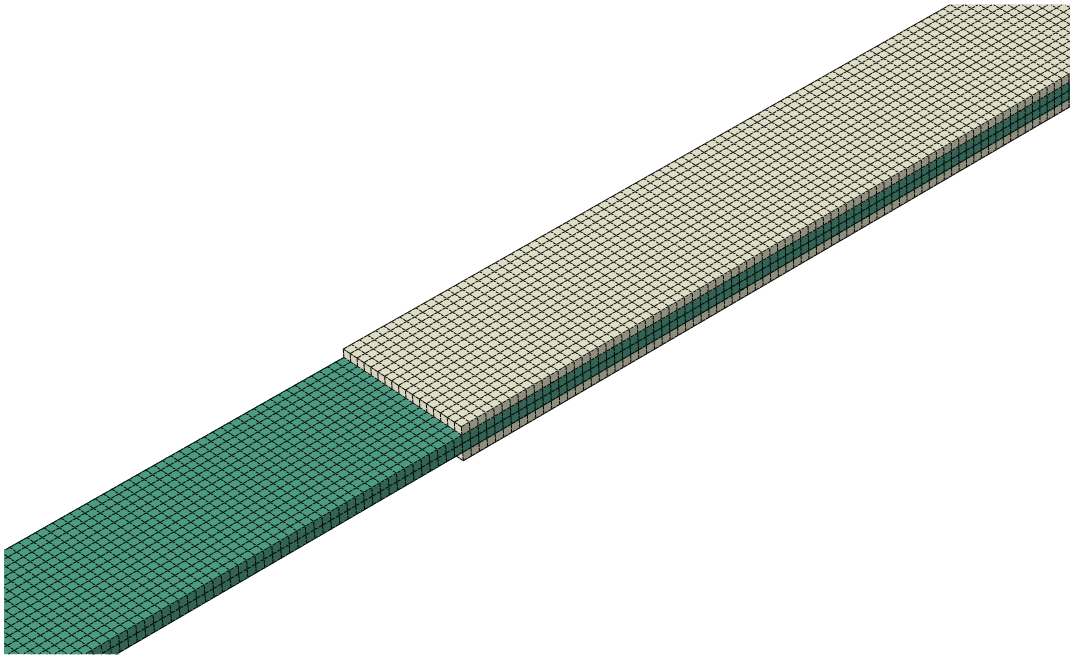

Fig.2. Meshed beam and piezoelectric layers.

(a)

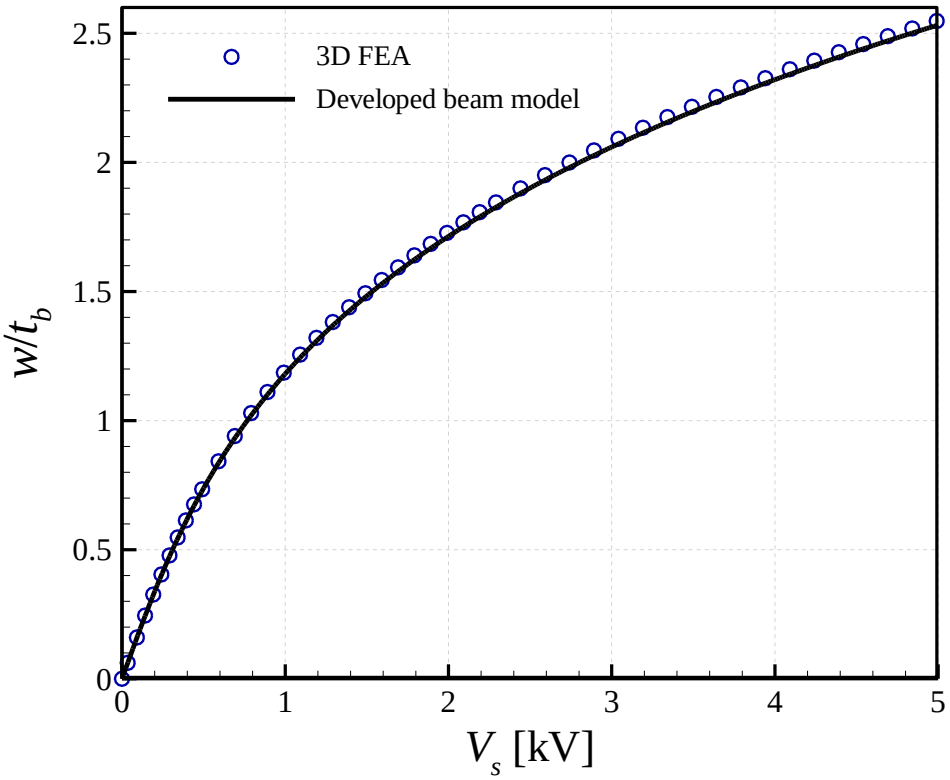

(b)

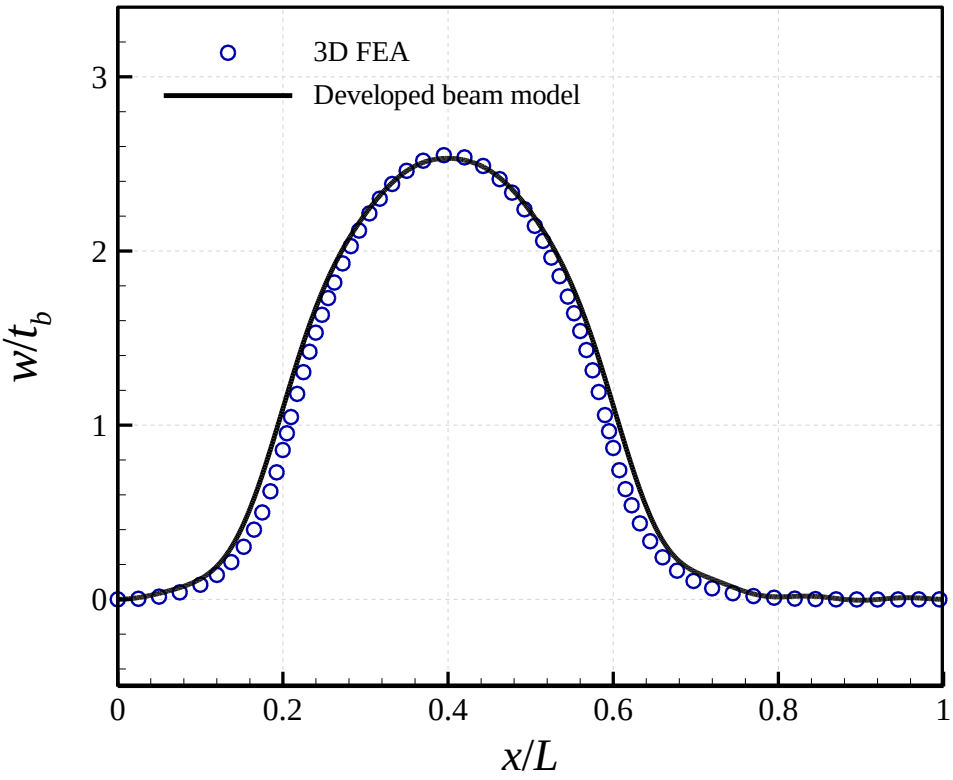

Fig.3. (a) The nonlinear transverse deflection at x/L=0.4 and (b) the nonlinear deformed configuration of the system at V_s=5 kV.

(a)

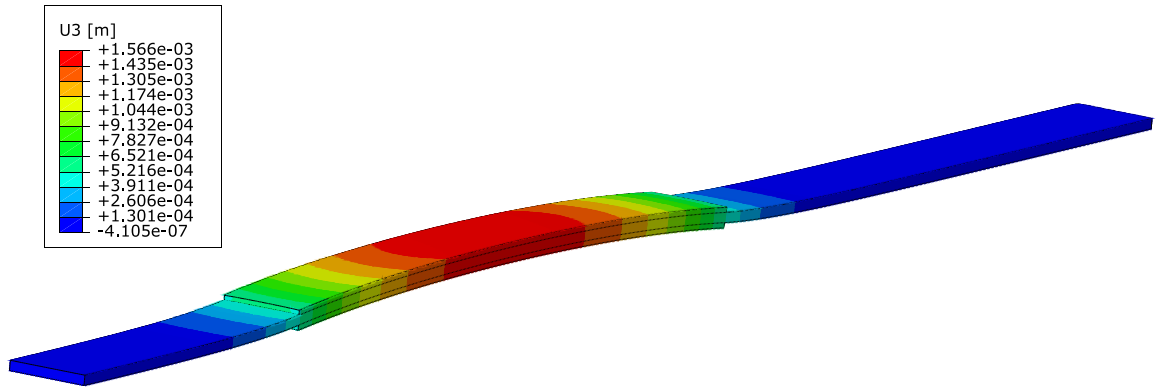

(b)

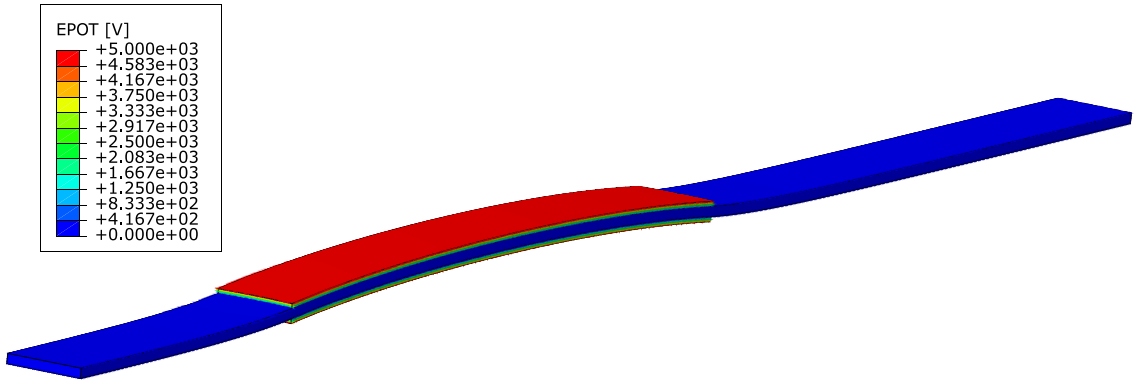

Fig.4. (a) Contour plots of the deflection in the transverse direction; (b) contour plots of the electric potential.

(a)

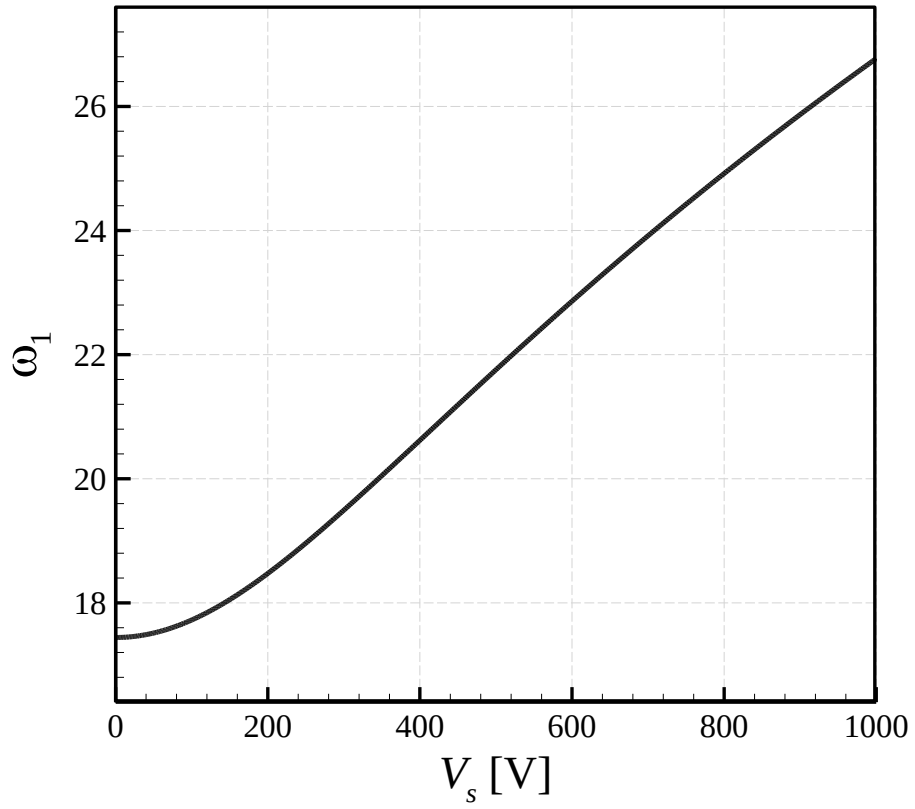

(b)

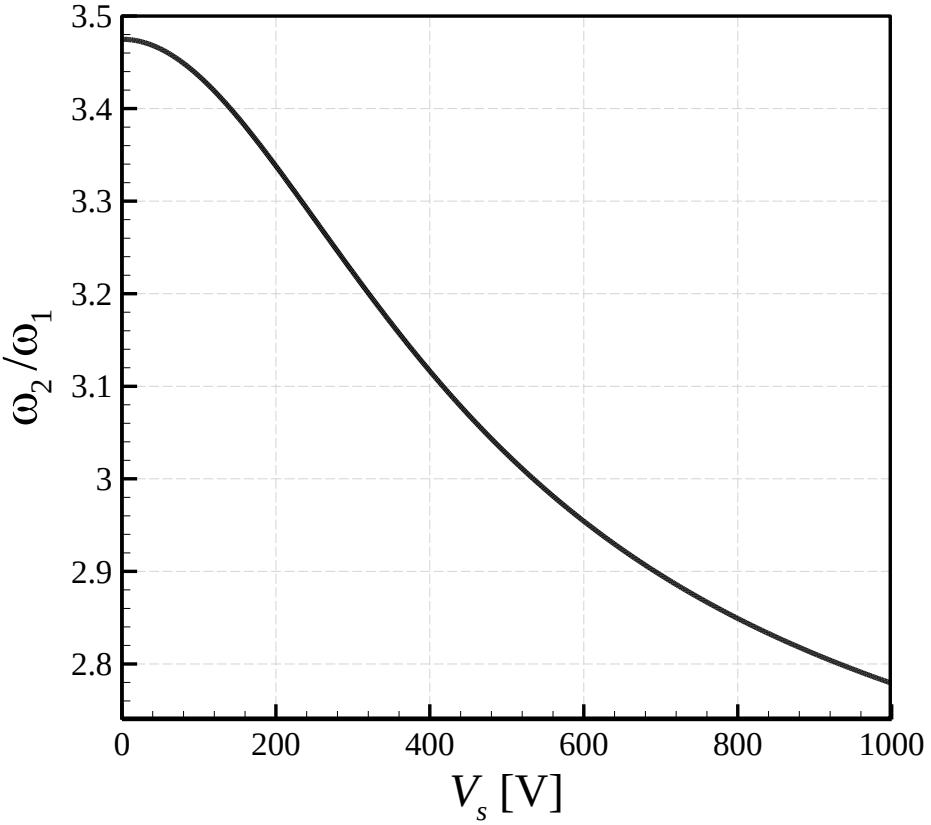

Fig.5. Variation of the (a) fundamental natural frequency and (b) ω_2/ω_1 ratio as a function of the DC input voltage V_s.

(a)

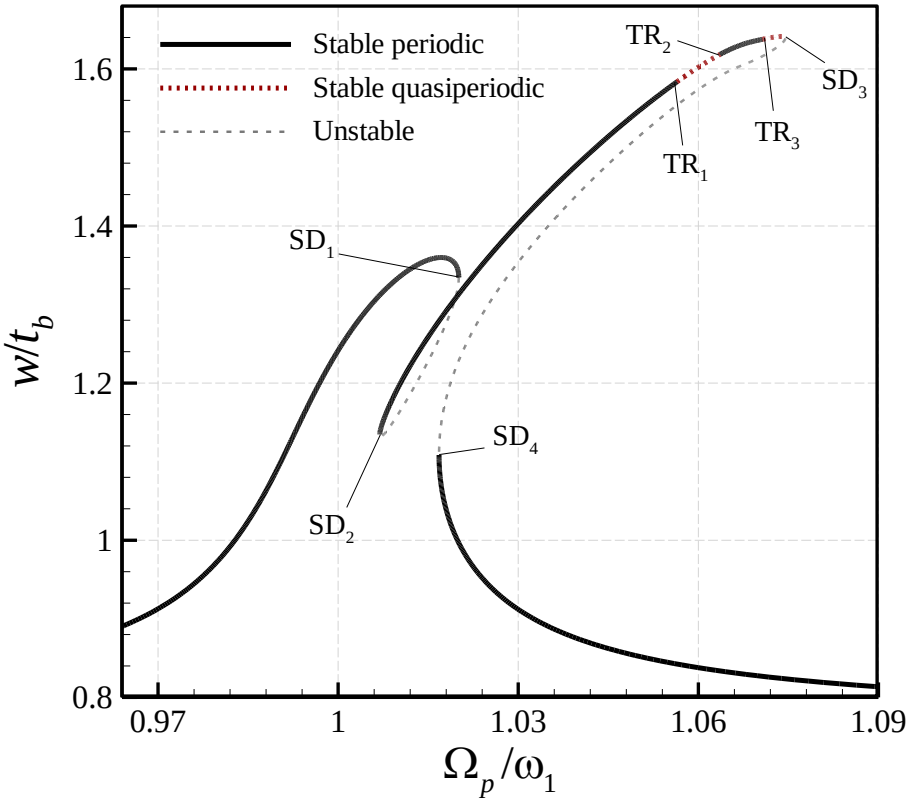
Stable periodic
Stable quasiperiodic
Unstable
TR2
SD3
TR3
TR1
SD1
SD4
SD2
1.6
1.4
1.2
1
0.8
w/tb
0.97
1
1.03
1.06
1.09
Ωp/ω1

(b)

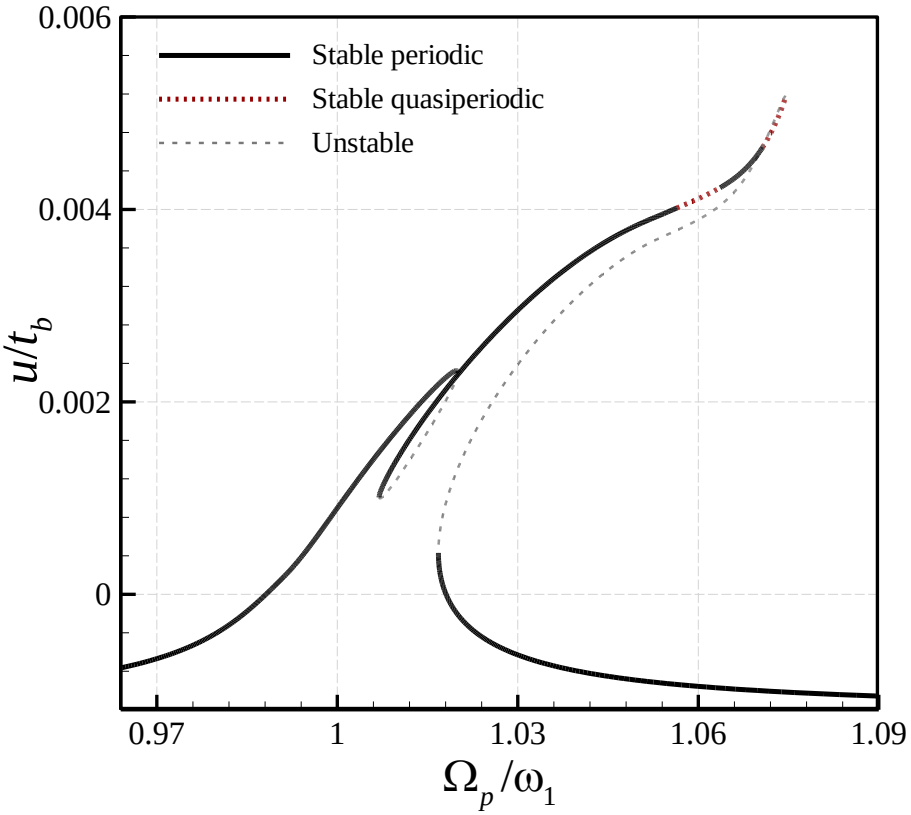
Stable periodic
Stable quasiperiodic
Unstable
0.006
0.004
0.002
0
u/tb
0.97
1
1.03
1.06
1.09
Ωp/ω1

(c)

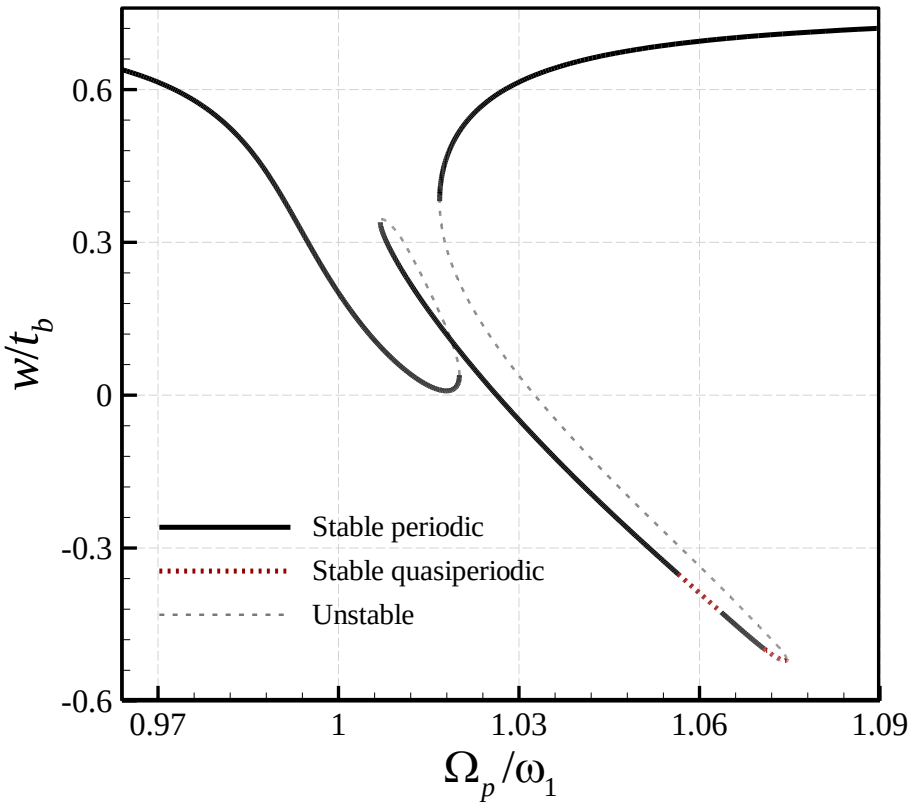

(d)

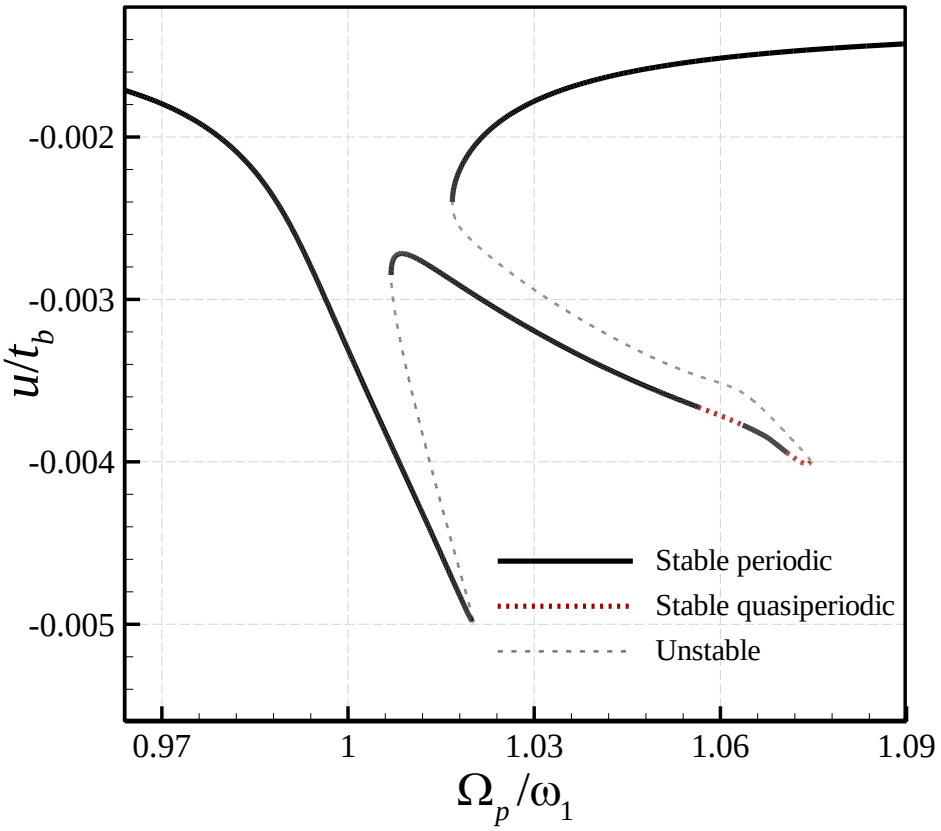

Fig.6. Resonance frequency-amplitude plots; (a) maximum of *w* at *x* =0.48 *L*; (b) maximum of *u* at *x*=0.47 *L*; (c, d) the counterparts of (a, b) for minimum displacement. V_d=10.0 V.

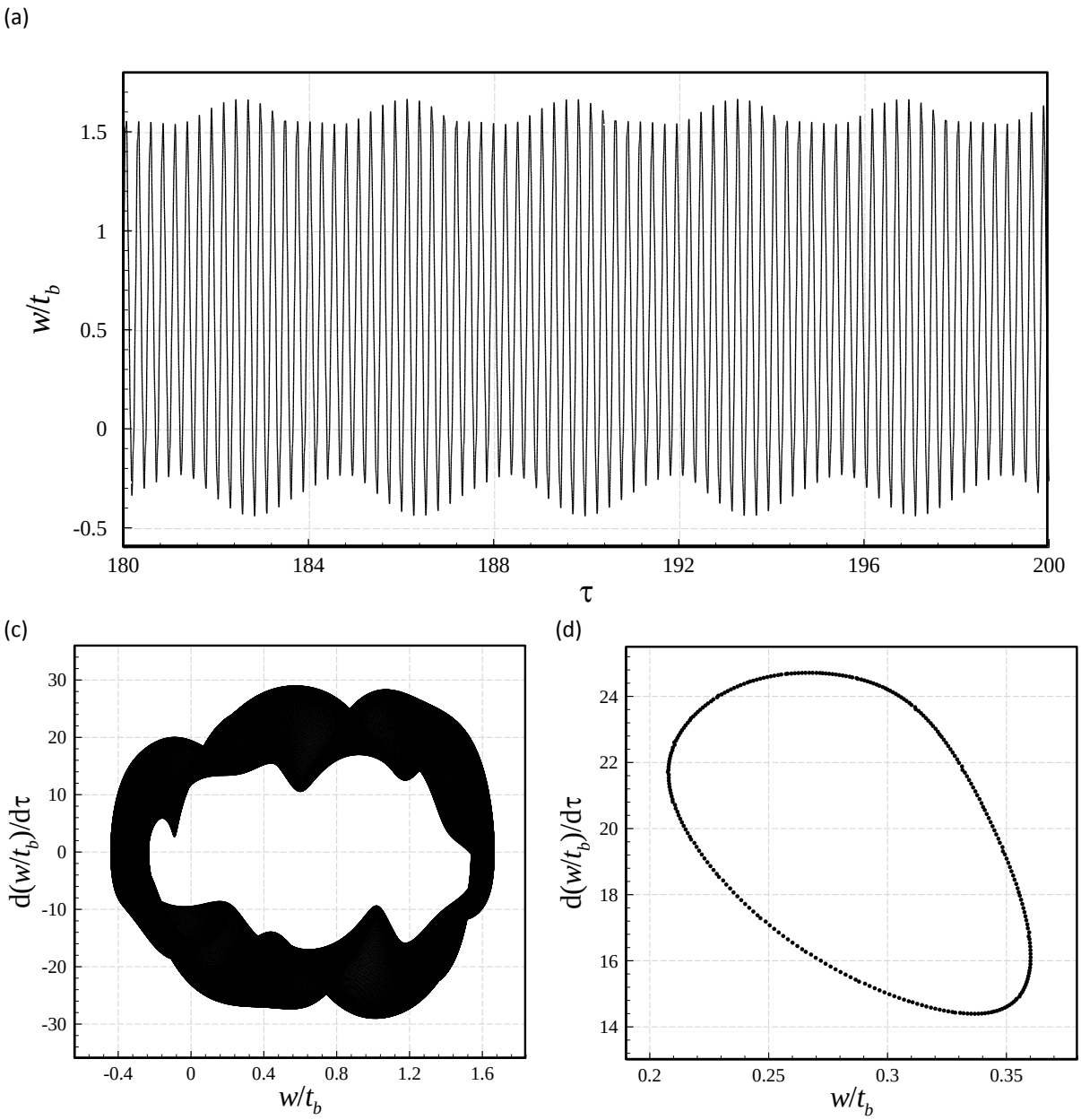

Fig.7. Details of the quasiperiodic motion of the system of Fig. 6 at Ω_p/ω_1=1.06; (a-c) time history, phase-plane, and Poincaré section of *w*.

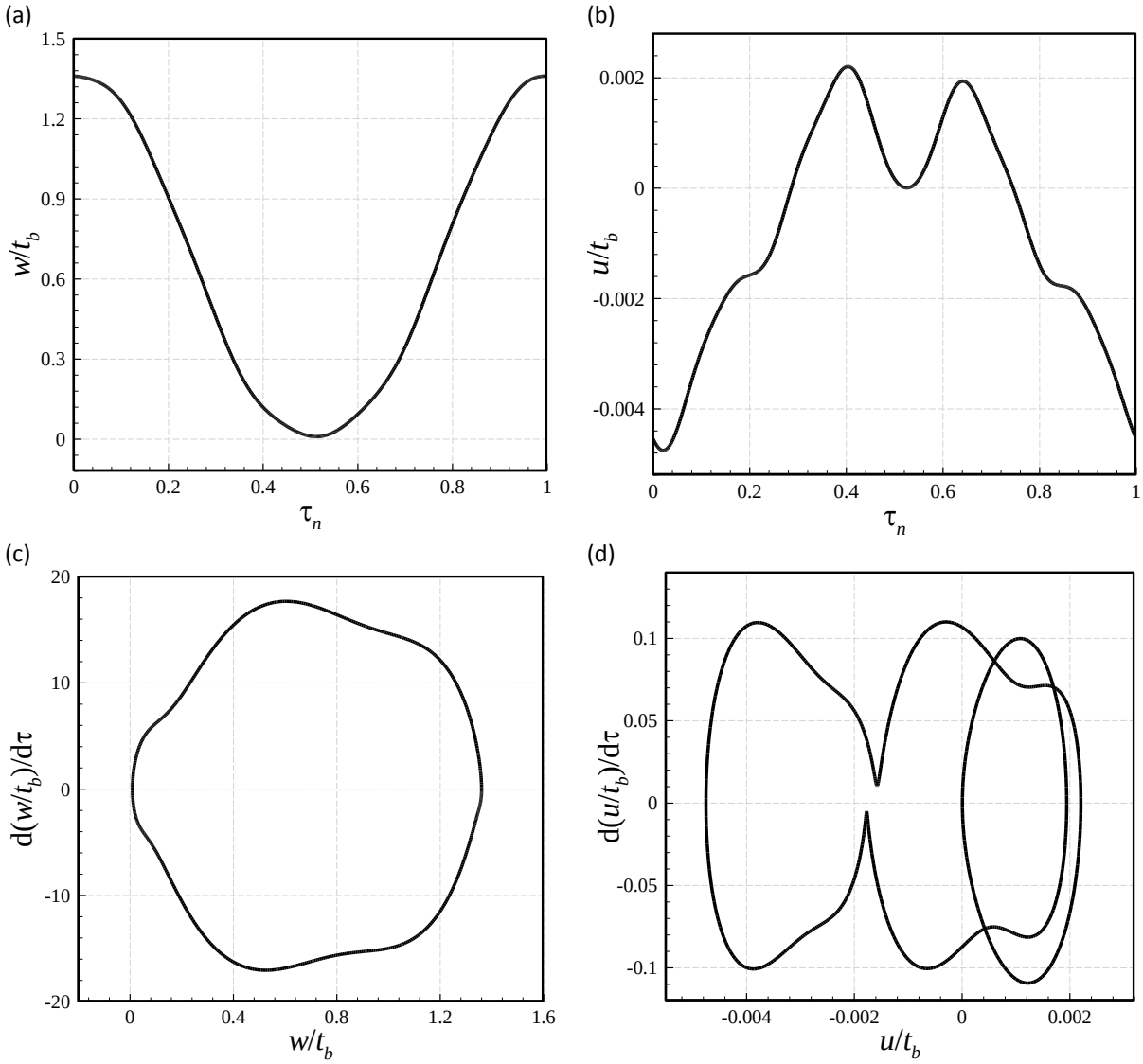

Fig.8. Details of the motion of the system of Fig. 6 at Ω_p/ω_1=1.0172; (a, b) time histories of the transverse and longitudinal displacements, respectively; (c, d) phase-plane portraits of the transverse and longitudinal displacement, respectively.

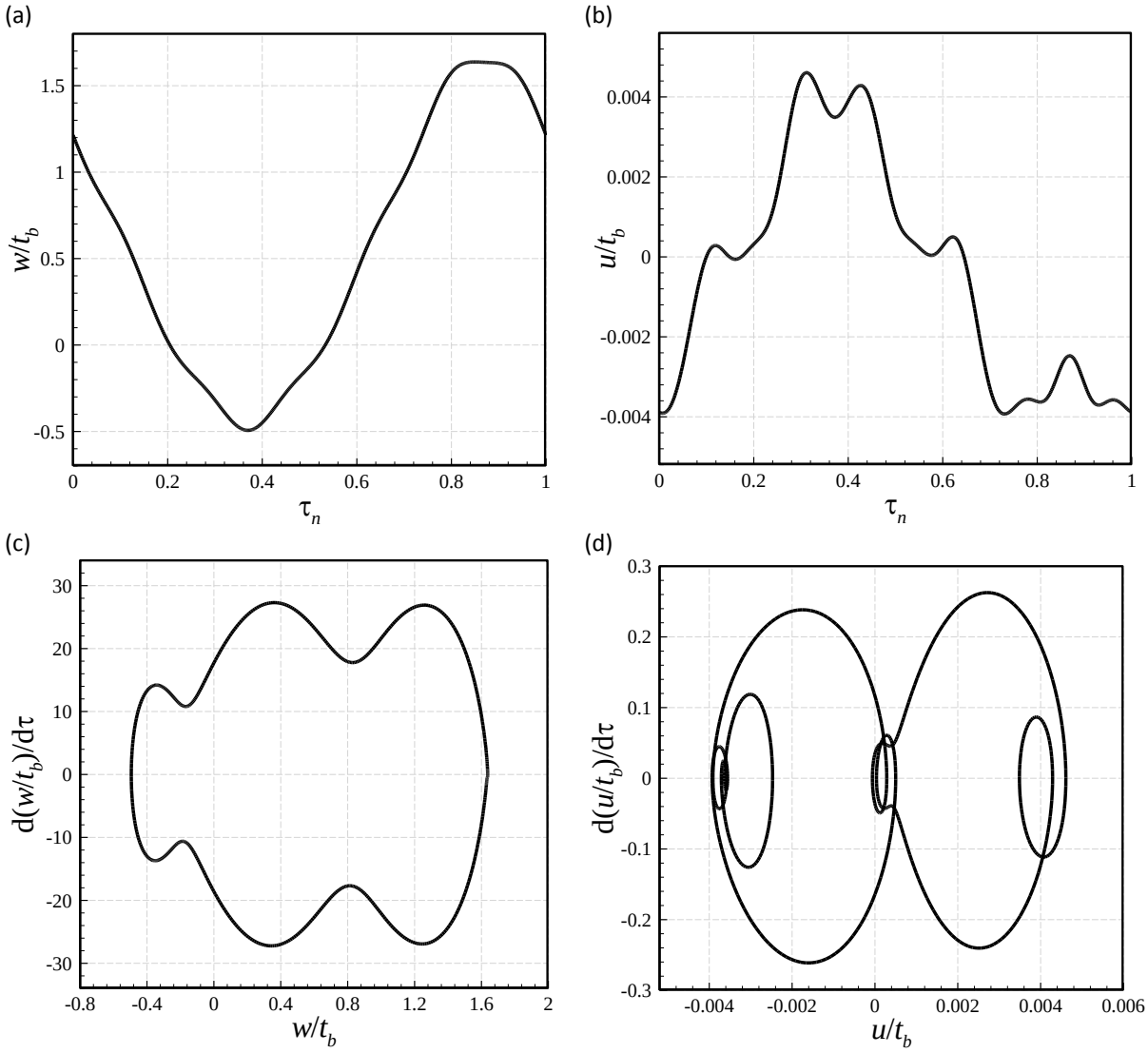

Fig.9. Details of the motion of the system of Fig. 6 at Ω_p/ω_1=1. 0703; (a, b) time histories of the transverse and longitudinal displacements, respectively; (c, d) phase-plane portraits of the transverse and longitudinal displacement, respectively.

(a)

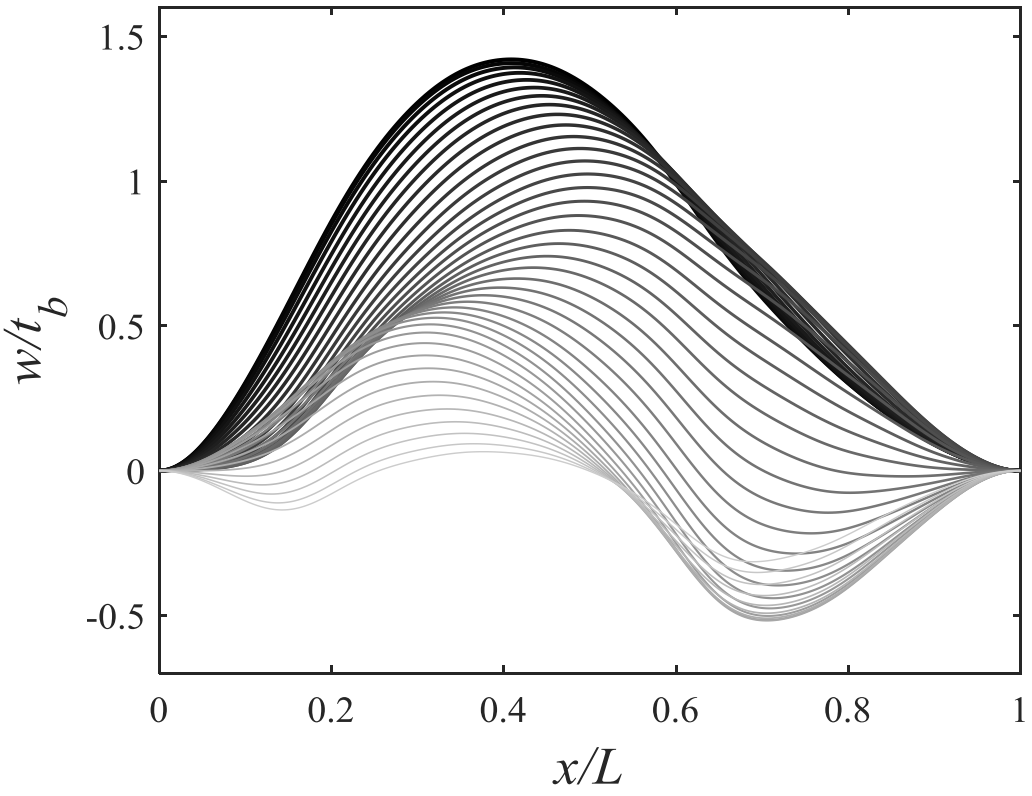

(b)

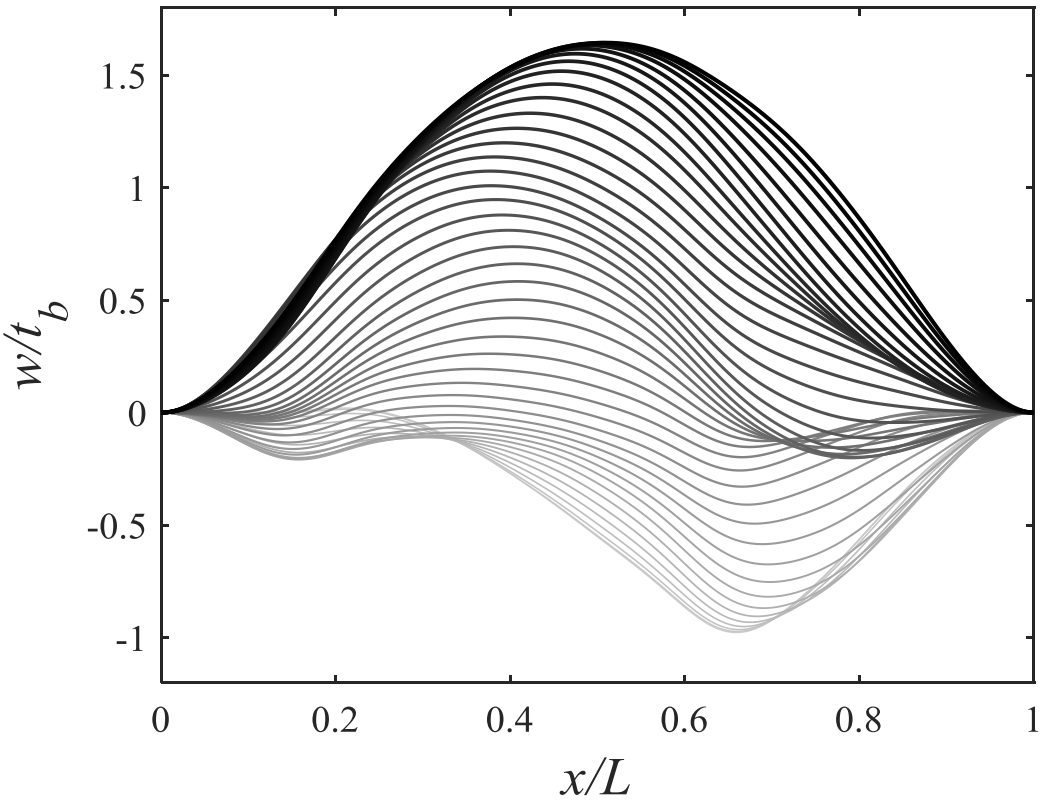

Fig.10. Transverse oscillation of the system of Fig. 6 in one period; (a) Ω_p/ω_1=1.0172; (a) Ω_p/ω_1=1.0703.

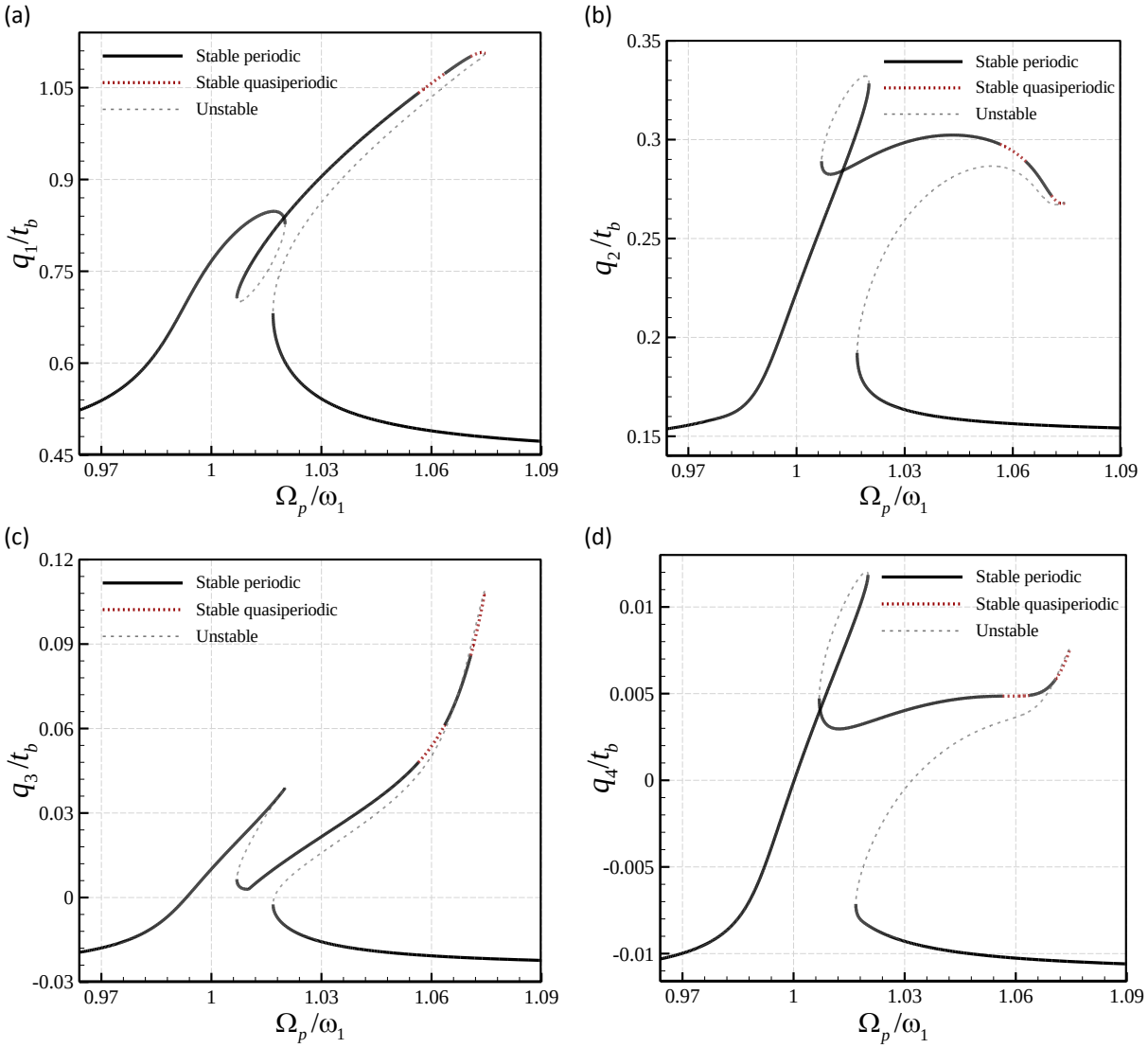

Fig.11. Resonance response of q_1, q_2, q_3, and q_4 of the system of Fig. 6.

(a)

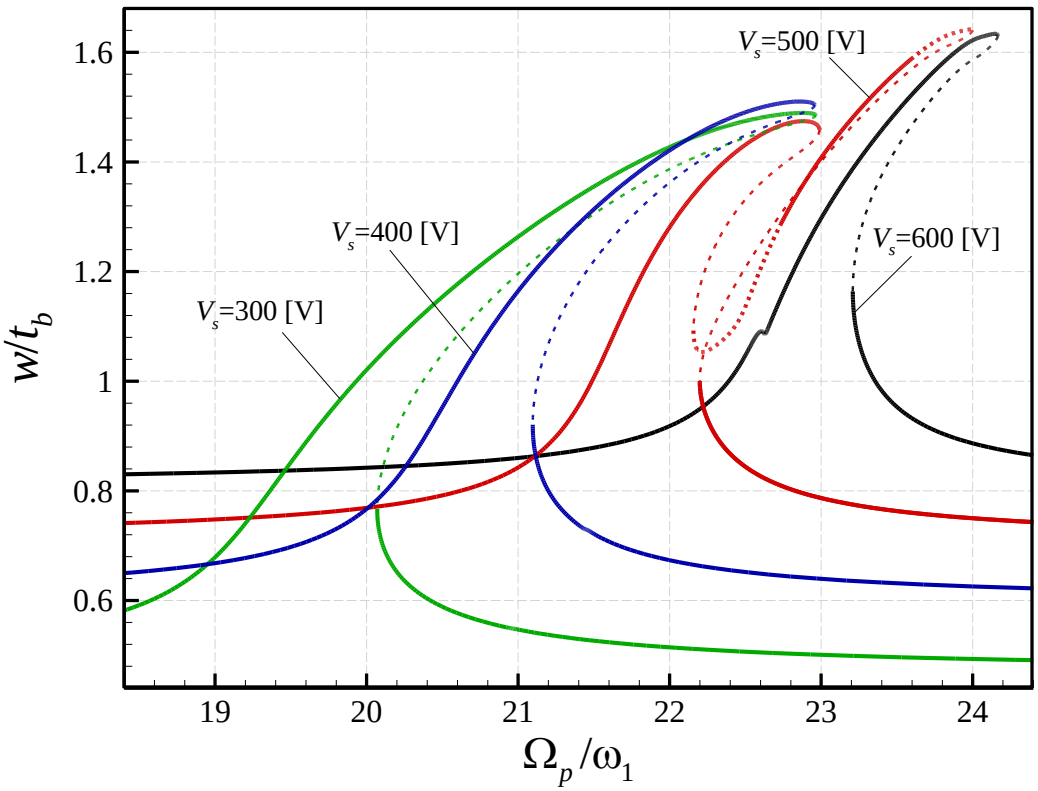

(b)

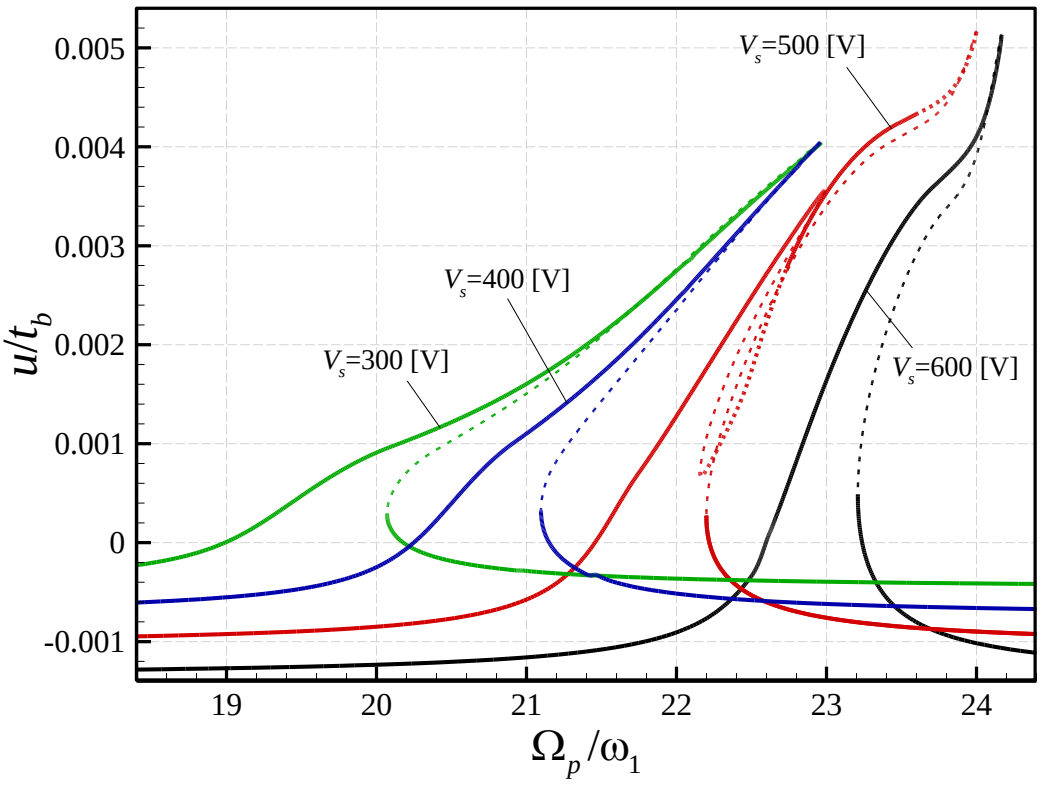

Fig.12. Effect of the DC voltage on the frequency-amplitude diagrams; (a) maximum of w at x=0.48 L; (b) maximum of u at x =0.47 L; V_d=10.0 V for all cases.

(a)

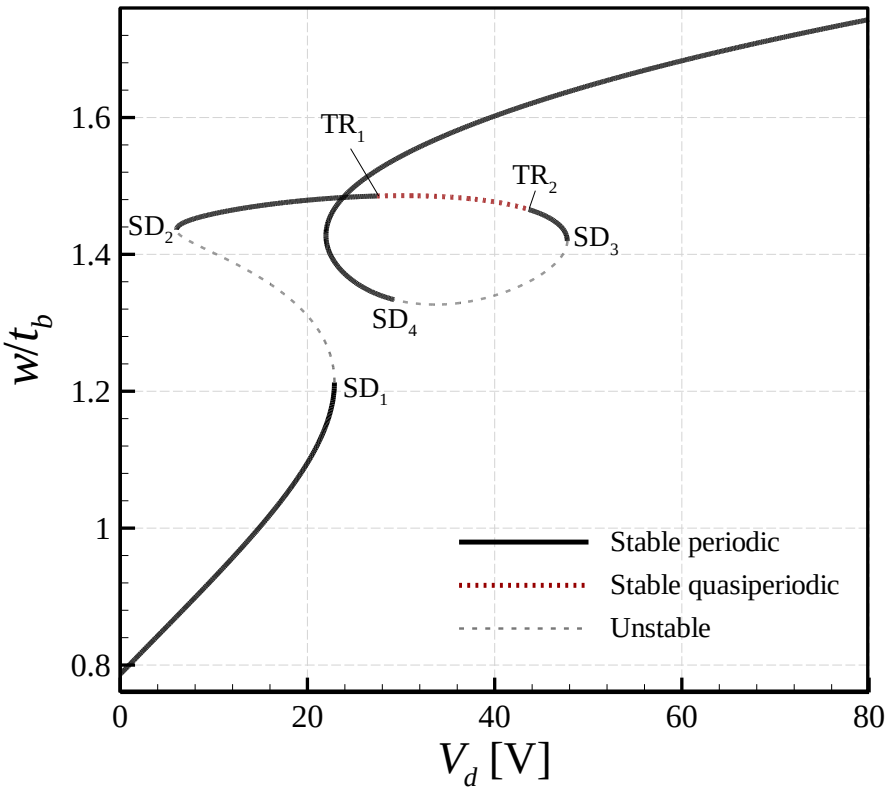
1.6
1.4
1.2
1
0.8
w/t_b
TR$_1$
TR$_2$
SD$_2$
SD$_3$
SD$_4$
SD$_1$
Stable periodic
Stable quasiperiodic
Unstable
0
20
40
60
80
V_d [V]

(b)

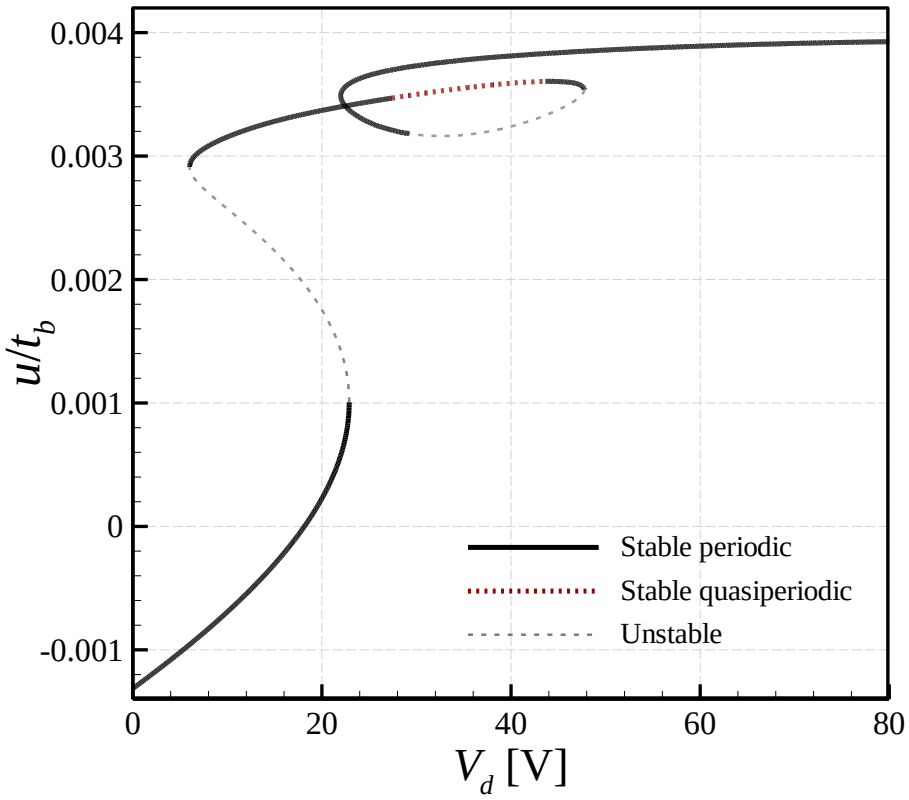
0.004
0.003
0.002
0.001
0
-0.001
u/t_b
Stable periodic
Stable quasiperiodic
Unstable
0
20
40
60
80
V_d [V]

(c)

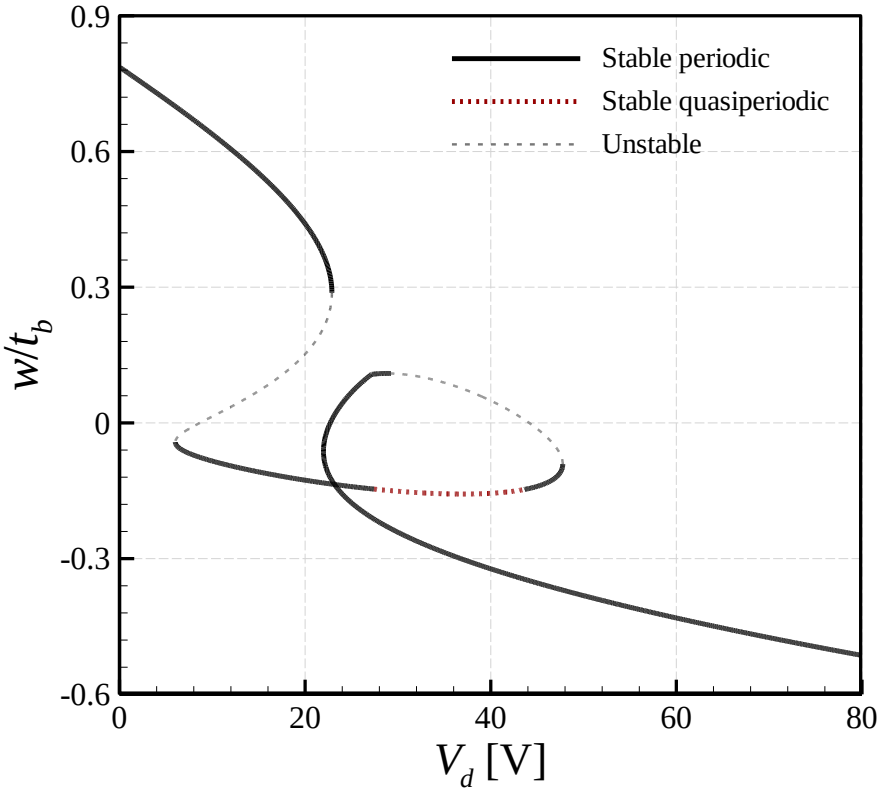

(d)

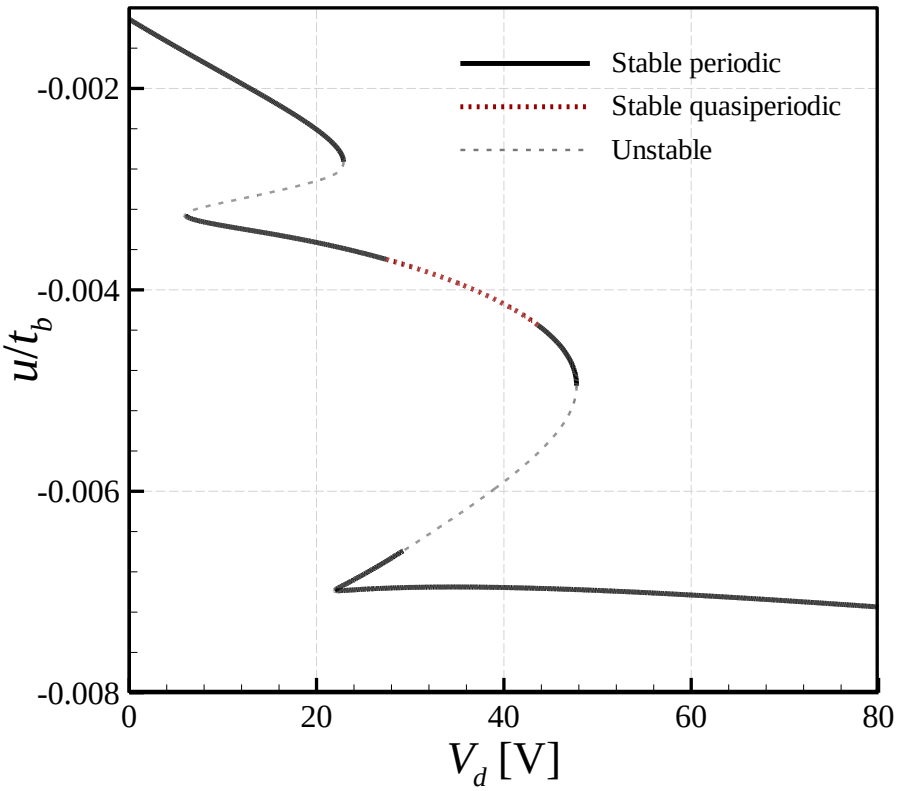

Fig.13. Resonance force-amplitude plots at Ω_p/ω_1=1.03; (a) maximum of *w* at *x*=0.48 *L*; (b) maximum of *u* at *x*=0.47 *L*; (c, d) the counterparts of (a, b) for minimum displacement. V_s=580 V.

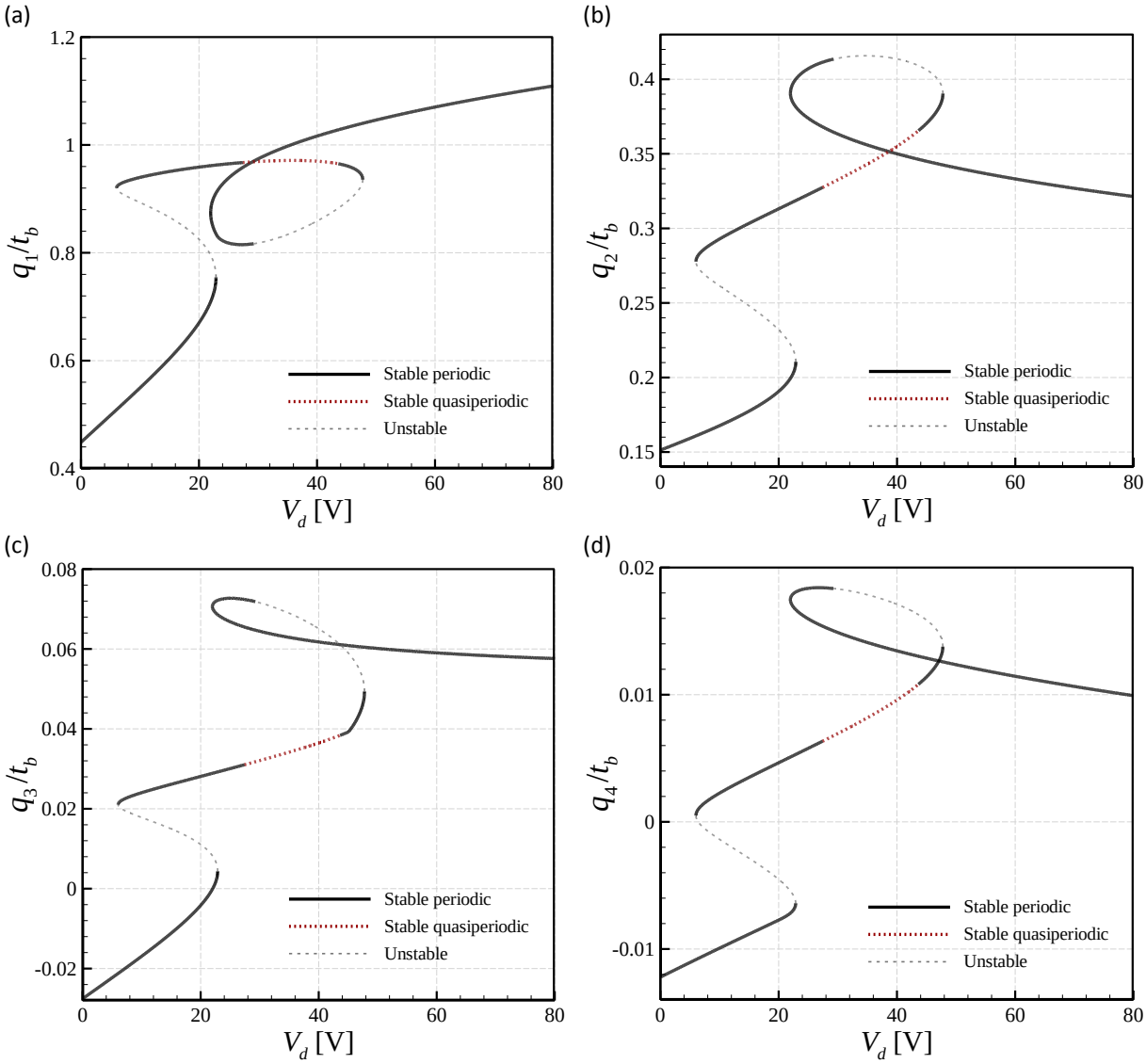

Fig.14. Force-amplitude plots of the generalised coordinates q_1, q_2, q_3, and q_4 of the system of Fig. 13.

(a)

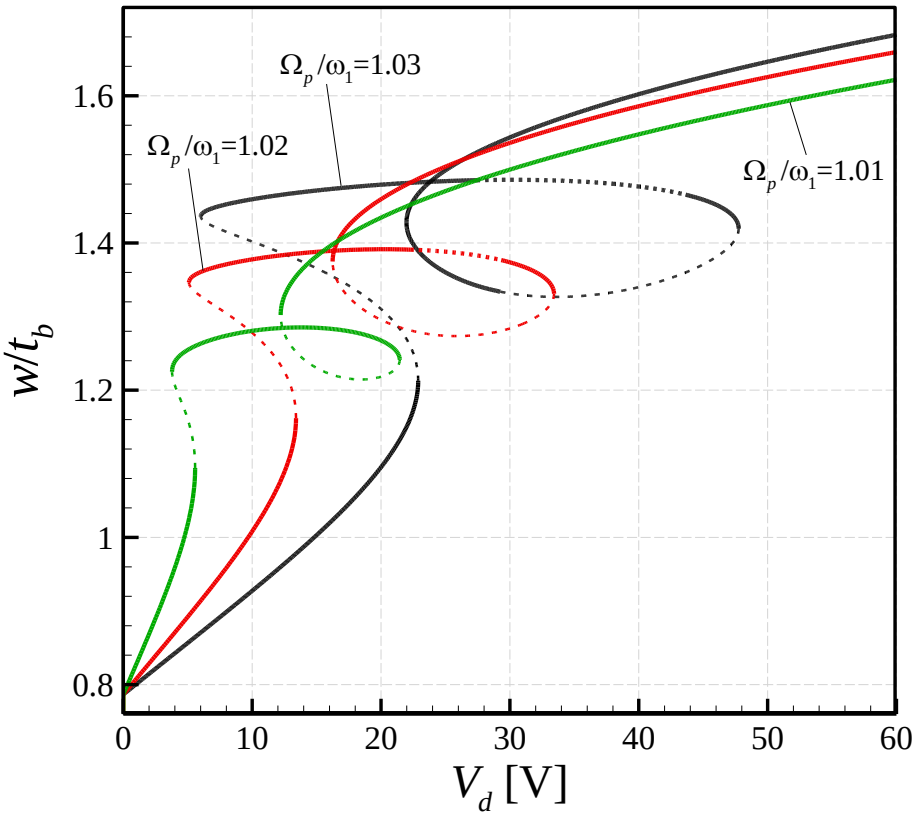

(b)

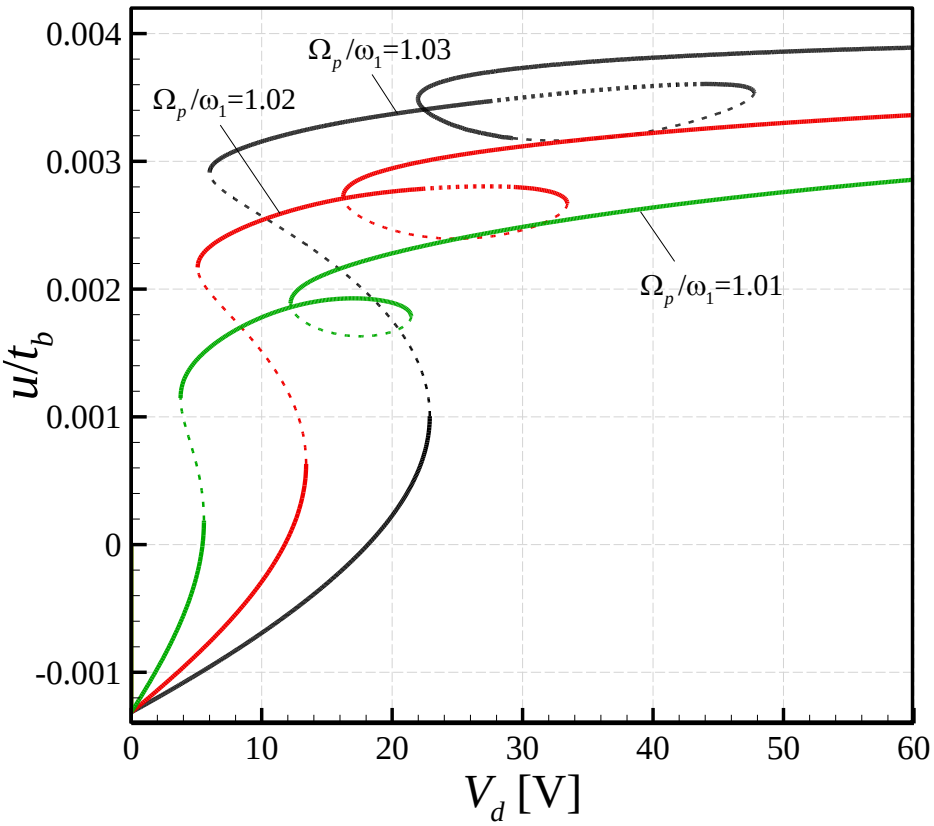

Fig.15. Resonance force-amplitude plots at different frequency ratios; (a) maximum of *w* at *x*=0.48 *L*; (b) maximum of *u* at *x*=0.47 *L*. V_s = 580 V.

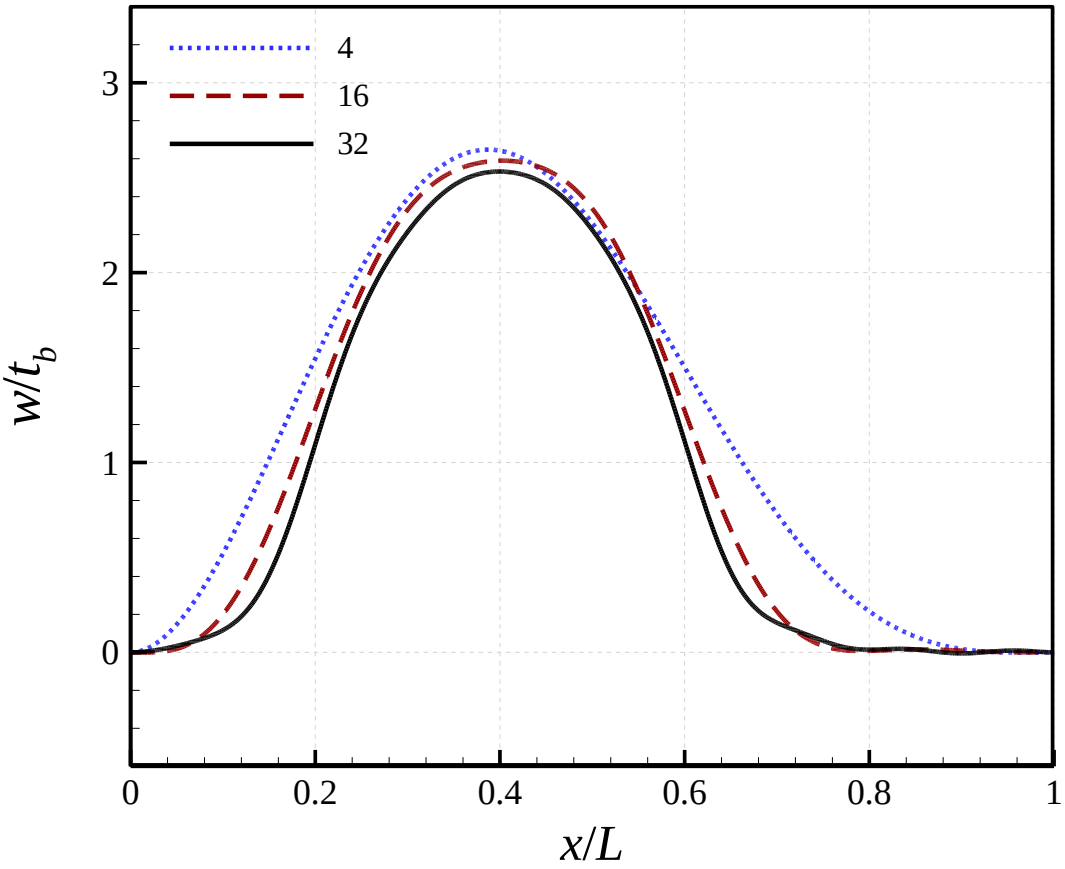

Fig.16. Effect of number of modes in the discretised model on nonlinear transverse deformation of the piezoelectrically actuated beam.